Journal of Structural Geology 177 (2023) 105006

Contents lists available at ScienceDirect

Journal of Structural Geology

journal homepage: www.elsevier.com/locate/jsg

MYflow - A simple computer program for rheological modelling of mylonites

Leonardo Casini [a,*], Matteo Maino [b], Ludovico Manna [b], Antonio Funedda [c]

[a] *Department of Chemistry, Physics, Mathematics and Natural Sciences, University of Sassari, 07100, Sassari, Italy*
[b] *Department of Earth and Environmental Sciences, University of Pavia, 27100, Pavia, Italy*
[c] *Department of Chemical and Geological Sciences, University of Cagliari, 09042, Cagliari, Italy*

ABSTRACT

In this study, we present a new Matlab-derived software, MYflow, developed to perform rheological modelling of high-strain rocks and mylonites. The software handles both monomineralic and compositionally heterogeneous rocks made of various proportions of the most common minerals such as quartz, feldspar, calcite, olivine, plagioclase, micas, pyroxene, amphibole and garnet. The rheology of composite mylonites is evaluated using a suite of mixing models combined with two complementary mechanical constraints derived from the assumption of either uniform stress or strain-rate. Various compositions can be used to run either 0th dimensional rheological models corresponding to classical strength profiles, or 2D maps showing the grain-scale spatial variability of stress and strain rate as a function of composition, grain size and effective deformation mechanism. The applicability of the code, along with its main functionalities, is demonstrated using a model of composite mylonite that reproduces the typical microstructure of rocks deformed in high-strain zones. The software is further benchmarked by modelling the grain-scale distribution of effective deformation mechanism, stress, and strain-rate of three natural mylonite developed under different pressure, temperature, and strain-rate conditions. The outcomes of our modelling approach are compared to the results obtained from classical paleopiezometry studies and evaluated in relation to the processes that yield to partitioning of stress and strain rate in shear zones. Finally, we discuss the significance of mean stress and strain rate in mylonites addressing the applicability of recrystallized grain-size paleopiezometry.

1. Introduction

Mylonites form within ductile or transitional brittle-ductile shear zones by extreme grain-size reduction in response to dynamic recrystallization (Bell and Etheridge, 1976; Lister and Price, 1978; Berthé et al., 1979; Simpson, 1985; Hirth and Tullis, 1992). In the past decades, several authors have increasingly recognized the contribution of various other processes such as fracturing, metamorphic reactions, and rigid-body rotation of grains (Handy 1994; Handy et al., 1999; Gomez-Barreiro et al., 2007; Miranda et al., 2016; Campbell and Menegon, 2019; Zhou et al., 2022). Therefore, in the remainder of this paper we refer to fine-grained high-strain rocks developed within shear zones as mylonites regardless of the relative contribution of dynamic crystallization to the bulk strain. The systematic association of mylonite and high-strain zones suggests that grain-size reduction is essential for weakening and localization of deformation (Fliervoet et al., 1997; Montesi and Hirth, 2003; Montesi 2007; Kilian et al., 2011; Platt and Behr, 2011b) and has also positive feedbacks on the seismicity and deep circulation of fluids through the ductile lower crust (Fusseis et al., 2009; Campbell and Menegon, 2019; Jamtveit et al., 2019), effectively controlling the rheological behaviour of the lithosphere (Précigout et al., 2007; Platt and Behr, 2011a, 2011b).

This apparent correlation makes mylonites sound geological archives that can be used to reconstruct complex pressure-temperature-time (P-T-t) deformation histories by combining microstructural analysis, geochronology and thermodynamic modelling (i.e., Langone et al., 2006; Brander et al., 2011; Campbell and Menegon, 2019; Corvò et al., 2022; Dumond et al., 2022; Casini et al., 2023). Mylonites also offer the opportunity of estimating differential stress under a wide range of P-T conditions and for various compositions through paleopiezometry, providing valuable information on the strength of the lithosphere below the brittle-ductile transition zone (i.e., Précigout et al., 2007; Campbell and Menegon, 2019).

However, paleopiezometric analysis based on the size of recrystallized grains or sub-grains has several drawbacks. First, the method is based on empirical calibrations developed for pure monomineralic aggregates (i.e., Twiss, 1977; Stipp and Tullis, 2003; Mehl and Hirth, 2008), whereas most mylonites are overall composite rocks with complex geometrical relationships between the constituting phases, so that only tiny domains can be considered effectively monomineralic (i.e., Casini and Funedda, 2014; Campbell and Menegon, 2019; Casini et al., 2021). This implies that the results obtained from recrystallized

---

* Corresponding author.
E-mail address: casini@uniss.it (L. Casini).

https://doi.org/10.1016/j.jsg.2023.105006
Received 23 May 2023; Received in revised form 8 November 2023; Accepted 14 November 2023

grain/sub-grain size paleopiezometry of mylonite would reflect, in most cases, very local stress values which likely do not fit neither the mean stress supported by the corresponding shear zone, nor that of the lithosphere (i.e., Vissers et al., 1995; Ortolano et al., 2020; Katori et al., 2021). Another important limitation is that the inverse relation between grain/sub-grain size and differential stress is mechanism dependent (Stipp et al., 2010). Thus, paleopiezometric analysis should be limited not only to compositionally homogeneous monomineralic domains, but also to those domains where the microstructure is consistent with the deformation mechanism the piezometer is calibrated for. After a few decades of studies combining both experimental (Dell'Angelo and Tullis, 1988; Rybacki et al., 2003; Rosenberg and Handy, 2005; Dimanov and Dresen, 2005; Dimanov et al., 2007; Cross and Skemer 2017) and theoretical approach (Voigt, 1928; Reuss, 1929; Tullis et al., 1991; Ji et al., 2003; Huet et al., 2014; Hobbs et al., 2019), it is now commonly accepted that the rheology of polymineralic aggregates may significantly deviates from that of monophase rocks, with severe implications for the lithosphere strength (Bürgmann and Dresen, 2008). One of the main reasons for such departure is perhaps the pinning of secondary phases which inhibits grain boundary diffusion and maintains the grain-size smaller than the equilibrium grain-size. Small grain-size promotes the switch from dislocation creep to grain boundary sliding (GBS) enhancing phase mixing, which results into further pinning, weakening, and high strain rates at relatively low stress as commonly deduced from the loss of crystallographic preferred orientation in fine-grained ultra-mylonite (Fliervoet et al., 1997; Casini and Funedda, 2014; Campbell and Menegon, 2019; Hobbs et al., 2019; Casini et al., 2023). Other possible processes include metamorphic reactions between different phases (Brodie and Rutter, 1987; Newman et al., 1999; Stünitz and Tullis, 2001) which release fluids and melts extending the stability of diffusion creep in composite rocks, supporting faster strain rates at relatively low stress (Tullis et al., 1991; Dijkstra et al., 2002). Yet, direct measurements of deviatoric stress levels are limited to the base of the brittle upper crust (Byerlee, 1978; Spann et al., 1991; McGarr, 1980; Zoback and Harjes, 1997), thus improving the rheological models of composite mylonite is necessary to properly extrapolate the strength of the lithosphere below the brittle-ductile transition zone.

In this paper, we illustrate a simple computer program (MYflow) designed for modelling the rheological behaviour of mylonites. A practical and user-friendly graphical user interface provides access to a database storing the physical parameters of the main rock-forming minerals, that can be combined with several mixing rules and two mechanical constraints to derive the flow law parameters of both monomineralic and composite mylonites. The mechanical constraints represent the viscous equivalent to the iso strain-rate (Voigt, 1928) and iso stress (Reuss, 1929) elastic bounds routinely applied to model the behavior of composite mylonite with heterogeneous composition, grain size, and spatially variable distribution of deformation mechanism (i.e., Huet et al., 2014; Hobbs et al., 2019). The software can be used to produce both classical 0th dimensional stress or strain-rate depth/temperature/grain-size profiles, as well as 2D stress or strain-rate distribution maps. The code is firstly demonstrated using a model microstructure representative of typical composite mylonites. The applicability of the software is further benchmarked by modelling the rheology and the effective deformation mechanisms of three natural mylonite samples for which robust crystallographic preferred orientation (CPO) or electron backscattered diffraction (EBSD) textural data, P-T conditions of deformation and paleopiezometric analysis are available, altogether with independently constrained estimates of regional strain rates (Casini and Funedda 2014; Katori et al., 2021; Zhang et al., 2022). Finally, the results obtained from our modelling approach are discussed in relation to stress and strain rate partitioning focusing on the significance and applicability of recrystallized grain size piezometers.

2. Theoretical background

2.1. Software architecture and main functionalities

MYflow is a user-friendly Matlab-derived software package designed to evaluate the viscous strength of mylonites. The program consists of a main graphical user interface (GUI) that controls the subroutines and the functions used to set up different rheological models, visualize the results, perform paleopiezometric analysis and export reusable graphics and excel tables (Fig. 1). The GUI also provides two scalable databases that store several paleopiezometric calibrations and the physical properties of most rock-forming minerals. These databases can be easily implemented by the user through a step-by-step procedure that allow incorporating new paleopiezometers or minerals, or modifying those already present in the databases through an easy procedure that can be accessed directly from the MYflow GUI. The mineral database (version dbm13_2022) includes quartz (Gleason and Tullis, 1995; Rutter and Brodie, 2004), K-feldspar (Chen et al., 2021), plagioclase (Mehl and Hirth, 2008), muscovite and biotite (Mares and Kronemberg, 1993), garnet (Karato et al., 1995), ortho- and clinopyroxene (Orzol et al., 2006; Dimanov et al., 2007; Cherniak and Dimanov, 2010; Moghadam et al., 2010; Bruijn and Skemer, 2014), olivine (Karato et al., 1980; Abramson et al., 1997; Hirth and Kohlstedt, 2003), calcite (Schmid et al., 1980; Rutter, 1995), magnetite (Till and Moskowitz, 2013), ilmenite (Hofmeister and Mao, 2003; Till and Rybacki 2020) and amphibole (Hacker and Christie, 1990; Cherniak and Dimanov, 2010). The database of paleopiezometric calibrations includes several piezometers derived for quartz (Twiss, 1977; Stipp and Tullis, 2003; Holyoke and Kronenberg, 2010; Shimizu, 2008), olivine (Twiss, 1977; Karato et al., 1980; van der Wal et al., 1993), calcite (Twiss, 1977; Schmidt et al., 1980; Rutter and Brodie, 2004), plagioclase (Twiss, 1977; Post and Tullis, 1999; Mehl and Hirth, 2008), feldspar (Speciale et al., 2022) and pyroxene (Bruijn and Skemer, 2014; Speciale et al., 2022). The rheology of both monomineralic and multiphase rocks composed of two or more mineral phases rocks is evaluated through 0th dimensional strength profiles showing the variation of stress or strain rate in a temperature/grain size space. The strength profiles obtained from these 0th dimensional models can be eventually compared with independent stress values obtained through paleopiezometric analysis. Deformation mechanism maps showing the stability field of dislocation creep, grain boundary sliding and diffusion creep at fixed temperature in stress/grain size space can also be computed for monomineralic models. Besides these classical projections, the software allow modelling the rheology of heterogeneous mylonite in 2D spaces showing the grain-scale distribution of stress, strain rate, and effective deformation mechanism. 2D models can be applied to monomineralic rocks with variable grain size,

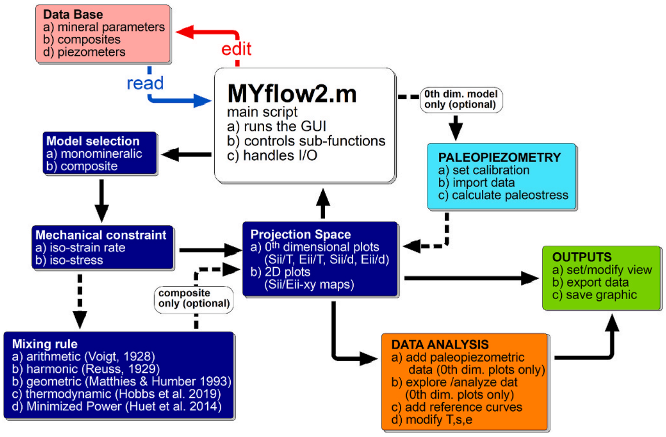

Fig. 1. Algorithm showing the main functionalities of software, the workflow, and the connection between different sub-routines.

or mylonite with variable composition and grain size.

2.2. Rules of mixture

The program implements five different rules of mixture to approximate the bulk rheology of compositionally heterogeneous mylonite. The first rule of mixture postulates that the strain rate is homogeneous (Voigt, 1928), the velocity field is continuous, and stress is homogeneous, but shear and normal stresses are discontinuous across the interfaces between the phases. Equivalently, the different phases within the composite aggregate are linked in parallel. Under these assumptions, the bulk viscosity of the aggregate is the arithmetic mean of the pure-phase viscosities, weighted by their volume fractions. Calling η_1 and η_2 the viscosities of the pure phases in a two-component aggregate and f_1 and $f_2 = 1 - f_1$ their volume fractions, the Voigt estimate of the macroscopic bulk viscosity η_{bulk} is:

$$\eta_{bulk} = f_1\eta_1 + f_2\eta_2 \tag{1}$$

Eq. (1) provides the upper bound of the viscosity of the composite (Paul, 1959). The second rule of mixture assumes that the internal stress is homogeneous and equal to the applied stress (Reuss, 1929). In this approximation, the normal and shear stress components acting on interfaces within the composite are continuous. Since the strain rate is homogeneous, the condition of velocity continuity is not satisfied at the interfaces of different components. This implies that the phases are connected in series, so that the strength of the composite is limited by the weakest phase and the bulk viscosity can be calculated from Eq. (2) as the harmonic average of the pure-phases viscosities:

$$\eta_{bulk} = \left(\frac{f_1}{\eta_1} + \frac{f_2}{\eta_2}\right)^{-1} \tag{2}$$

This approximation represents the lowest bound for the bulk viscosity of the mixture (Paul, 1959).

The third rule of mixture uses the geometric average and provide a more conservative estimate of composite strength usually in good agreement with experimental results (Matthies and Humbert, 1993; Ji et al., 2003; Ji 2004). The minimized power geometric mean is based on the minimization of the mechanical power dissipated during viscous deformation and provides a simple analytical formulation of the flow properties of composites with phases characterized by large viscosity contrast (Huet et al., 2014). Finally, the thermodynamic mixing law models the bulk strength of composite based on the Arrhenius logarithmic relation which accounts for the molar proportion of different grain sizes or different minerals deforming by a given process (Hobbs et al., 2019).

2.3. Modelling strategy

The program combines a phenomenological approach based on setting viscous bounds derived from external independent constraints (i.e., Voigt, 1928; Reuss, 1929) and a criterion of minimization of the mechanical power (i.e., Jiang et al., 2005; Huet et al., 2014). Our modelling strategy grounds on two basic assumptions. The first implies that the creep of any ideal polycrystalline, single-phase, material with homogeneous grain size involves one deformation mechanism and could be described by an Arrhenius-type relationship of the form:

$$\begin{cases} \dot{\varepsilon} = \beta\mu^n d^{-m} \\ \beta = A\exp\left(-\dfrac{Q}{RT}\right) \end{cases} \tag{3}$$

where $\dot{\varepsilon}$ is strain rate [s^{-1}], μ is the differential stress [MPa], d is the grain size [μm], R is the gas constant equals to 8.314 $Jmol^{-1}K^{-1}$ and T is the temperature [K]. The pre-exponential constant A [$MPa^{-n}\mu m^{-m}\ s^{-1}$], the stress exponent n [dimensionless], the activation enthalpy Q [$Jmol^{-1}$], and the grain size exponent m [dimensionless] are parameters that characterize the viscous response of the material. Mechanism-dependent flow laws for monomineralic rocks composed of one of the various minerals included in the database are formulated from Eq. (3) using experimentally derived parameters such as pre-exponential constant of dislocation creep (A_{DC}) and the activation enthalpies for dislocation motion (Q_D) and grain boundary diffusion (Q_{diff}) and taking stress and grain size exponents of dislocation creep, diffusion creep and grain boundary sliding as specified in Table 1. Equation (1) does not account for water fugacity, which has been included in the formulation of a few flow laws recently developed for quartz (i.e., Stipp et al., 2006; Tokle et al., 2019). Although water contained in hydrous phases or, more in general, the hydrogen or fluoride content of nominally anhydrous minerals likely influences the flow of mylonite, the value of the water fugacity exponent is still poorly constrained and generally not available except for quartz and few other phases. Therefore, we explicitly neglect the water fugacity term in Eq. (1).

The pre-exponential constants of diffusion creep (A_{Diff}) and grain boundary sliding (A_{GBS}) are calculated based on the following equivalences (Langdon and Mohamed, 1976; Hobbs et al., 2019):

$$\begin{cases} A_{Diff} = \left(82G^3b^3/3\right)A_{DC} \\ A_{GBS} = \left(10G^2b^2/3\right)A_{DC} \end{cases} \tag{4}$$

In the group of equation (2), A_{DC} is the experimentally constrained pre-exponential constant of dislocation creep, G is shear modulus [MPa], and b is the Burgers vector [mm]. The second assumption is that different deformation mechanisms work cooperatively to minimize the amount of mechanical work dissipated by heterogeneous mylonite (i.e., Huet et al., 2014; Hobbs et al., 2019). In a viscous material, strain rate and deviatoric stress are related by viscosity η [Pas] according to the relation:

$$\mu = 2\eta\dot{\varepsilon} \tag{5}$$

The effective viscosity for both linear and power law homogeneous material can be formulated in terms of stress (η_μ) or strain rate ($\eta_{\dot{\varepsilon}}$) by combining Eq. (3) and Eq. (5), as:

$$\begin{cases} \eta_\mu = \dfrac{\mu^{1-n}}{2\beta d^{-m}} \\ \eta_{\dot{\varepsilon}} = \dfrac{\dot{\varepsilon}^{\frac{1-n}{n}}}{2\beta^{\frac{1}{n}} d^{-\frac{m}{n}}} \end{cases} \tag{6}$$

Neglecting for simplicity the isotropic component of the strain energy function, the mechanical power $\dot{W}$ [Pas^{-1}] associated to viscous deformation of a homogeneous material can be formulated for strain rate ($\dot{W}_{\dot{\varepsilon}}$) or stress ($\dot{W}_\mu$), respectively, as (Ranalli, 1995):

$$\begin{cases} \dot{W}_\mu = \mu^2/2\eta \\ \dot{W}_{\dot{\varepsilon}} = 2\eta\dot{\varepsilon}^2 \end{cases} \tag{7}$$

which can be re-formulated substituting eq. (6):

$$\begin{cases} \dot{W}_\mu = \mu^{1+n}\beta d^{-m} \\ \dot{W}_{\dot{\varepsilon}} = \dfrac{\dot{\varepsilon}^{\frac{1+n}{n}}}{\beta^{\frac{1}{n}} d^{-\frac{m}{n}}} \end{cases} \tag{8}$$

The assumption of cooperative behavior implies that deformation mechanisms operate in parallel (Mohamed and Langdon, 1975), thus the bulk strain rate $\dot{\varepsilon}_{bulk}$ of an aggregate is expressed as the sum of the partial

Table 1
Flow law parameters.

mechanism	A	n	m	Q
dislocation creep	A_{DC}	4	0	Q_D
diffusion creep (Coble)	$(82G^3b^3/3)A_{DC}$	1	3	Q_{diff}
grain boundary sliding	$(10G^2b^2/3)A_{DC}$	2	2	

strain rates accommodated by dislocation creep ($\dot{\varepsilon}_{DC}$), solid-state diffusion creep ($\dot{\varepsilon}_{Diff}$) and grain boundary sliding ($\dot{\varepsilon}_{GBS}$) as:

$$\dot{\varepsilon}_{bulk} = \dot{\varepsilon}_{DC} + \dot{\varepsilon}_{Diff} + \dot{\varepsilon}_{GBS} \tag{9}$$

The composition of the aggregate consists of N different phases and a total of n grains such that the volume proportion between phases φ_i and the number of grains of a given phase φ_i define the following equivalences:

$$\begin{cases} \varphi_i = 1 - \sum\limits_{j \neq i} \varphi_j \\ \varphi_i = n - \sum\limits_{j \neq i} \varphi_j \end{cases} \tag{10}$$

Provided that each grain within the aggregate deforms through only one deformation mechanism at a time, the bulk mechanical power $\dot{W}_{bulk}$ dissipated by a compositionally and geometrically heterogeneous mylonite can be calculated from the statistical thermodynamics of regular cooperative assemblies (Fowler and Guggenheim 1949; Hobbs et al., 2019) by combining Eq. (10) and Eq. (8) and summing the mechanical power dissipated in each grain weighted by the molar volume proportion V_i of the corresponding phase in the aggregate, as:

$$\dot{W}_{bulk} = \sum_i \sum\nolimits_{k=1}^{\varphi_i} \left(\dot{W}_{\dot{\varepsilon}}, \dot{W}_{\mu}\right)_k \frac{\varphi_i \prod\limits_{j \neq i} V_j}{\sum\limits_i \varphi_i \prod\limits_{j \neq i} V_j} \tag{11}$$

If the different deformation mechanisms operate independently of each other the local values of mechanical power do not influence the rate of mechanical power dissipation in the rest of the aggregate. Therefore, Eq. (11) can be used in combination with a mechanical constraint such as iso-strain (Voigt, 1928) or iso-stress (Reuss, 1929) to determine the local effective deformation mechanism by computing from Eq. (3) the minimum potential stress or strain-rates related to dislocation creep, diffusion creep and grain boundary sliding.

2.4. Paleopiezometry

Stress estimates based on the grain size of recrystallized aggregates can be calculated from paleopiezometric calibrations formulated as (i.e., Twiss, 1977):

$$\mu = \theta d^{-p} \tag{12}$$

where θ is a constant that depends on the mineral the calibration is set for, d is grain size expressed as the diameter of the area-equivalent circle [μm], and the grain size exponent p generally takes a value slightly larger than unity (Twiss, 1977; van der Wal et al., 1993; Stipp and Tullis, 2003; Ter Heege et al., 2004a,b; Mehl and Hirth, 2008; Shimizu, 2008). The results computed from Eq. (12) are shown in a table and could be eventually displayed along with the strength profiles and other references envelope in the main plot while working with 0th dimensional models.

It should be emphasized that paleopiezometry based on Eq. (12) can be applied only to compositionally homogeneous aggregates as the presence of secondary phases promotes pinning, stabilizing small grain size not in equilibrium with the flow stress (Zener, 1951). Deformation mechanism maps constructed under a wide range of temperature for various minerals show that dislocation creep switch into diffusion creep, grain boundary sliding, or a combination of both processes, once the grain size reaches a critical value (i.e., Précigout et al., 2007; Mehl and Hirth, 2008; Shimizu, 2008; Hobbs et al., 2019). This implies that mylonite with heterogeneous grain size distribution is also expected to deform by multiple deformation mechanism at a time, making Eq. (12) applicable only to monomineralic domains with uniform grain size (Stipp et al., 2010). The program MYflow provides a way around these limitations, as the mean stress of composite mylonite with heterogeneous microstructure can be derived from 2D microstructural maps using the cumulative sum of molar volume weighted grain stresses, each calculated from Eq. (3) by substituting the parameters corresponding to the effective deformation mechanism operating within each grain. Provided V_j and Vm_j represent the volume proportion and the molar volume of the j^{th} phase in a mineral aggregate composed of n grains and N different phases, respectively, the mean stress $\overline{\mu}$ and mean strain rate $\overline{\dot{\varepsilon}}$ are calculated as:

$$\begin{cases} \overline{\mu} = \sum\limits_{i=1}^{n} \mu_i \dfrac{\alpha S_i}{A} \\ \overline{\dot{\varepsilon}} = \sum\limits_{i=1}^{n} \dot{\varepsilon} \dfrac{\alpha S_i}{A} \end{cases} \tag{13}$$

$$\alpha = \frac{V_j \prod\limits_{k \neq j} Vm_k}{\sum\limits_{j=1}^{N} V_j \prod\limits_{k \neq j} Vm_k} \tag{14}$$

where A is the total area of the composite mylonite analysed in the 2D map, S_i, and μ_i represent the grain surface and local stress, respectively. Of course, to obtain reliable stress values the analysed mylonite should contains a statistically meaningful number of grains defined based on the average grain size of the rock (i.e., Lopez-Sanchez and Llana-Funez, 2015).

3. Application to a model microstructure

3.1. Experimental set up

The program is demonstratively applied to a composite ultra-mylonite made of highly mixed phases. The model microstructure represents a compositionally heterogeneous ultra-mylonite made of three phases A, B, and C (Fig. 2a) with volume fractions $\varphi_A = 0.84$, φ_B 0.13 and φ_B 0.03, respectively (Fig. 2b). The various phases are highly mixed, and their grain size distribution is almost uniform, giving way to an overall compositionally homogeneous rock at the thin section scale. The rheology of the three phases is set using the physical parameters of dry anorthite (phase A), pyroxene (phase B) and amphibole (phase C) to simulate the behaviour of mafic mylonite deformed at HT-UHT conditions (T > 800–900 °C) in the lower crust or uppermost mantle (Sibson, 1980; Platt and Behrmann, 1986; Casini et al., 2021; Précigout et al., 2017). In a first set of experiments assuming an iso-strain rate condition, we evaluate the variation of stress and the distribution of deformation mechanisms for variable strain rates between 1×10^{-6} s^{-1} to 1×10^{-10} s^{-1}. The second set of experiments analyses the dependence of strain rate on stress and the change of deformation mechanisms under the assumption of uniform stress in the range 1–100 MPa. All experiments were replicated using a temperature of either 750 °C or 850 °C.

3.1.1. Distribution of stress and strain rate

The first set of experiments assuming an iso-strain rate condition shows that stress is only moderately partitioned between the various mineral phases of the model mylonite. At temperature of 850 °C, the highest strain rate of 1×10^{-6} s^{-1} corresponds to average stress of 26.8 MPa and peak stress of 83.0 MPa, localized within anorthite (Fig. 3a). Stress decays for decreasing strain rates and become vanishingly small (<1 MPa) at the lowest strain rate used in the experiments 1×10^{-10} s^{-1} (Fig. 3b and c). The low temperature runs show a similar near-logarithmic decrease of stress recording average values of 210.2 MPa at 1×10^{-6} s^{-1}, 30.7 MPa and 2.8 MPa at 1×10^{-8} s^{-1} and 1×10^{-10} s^{-1}, respectively (Fig. 3d–f). On the other hand, the experiments at iso-stress conditions result into localization of deformation, as the strain rate recorded by hornblende is up to 4 orders of magnitude higher than that of the stronger anorthite + diopside aggregate (Fig. 3g-l). At 850 °C, in fact, 1 MPa corresponds to an average strain rate of $1 \times 10^{-15.2}$ s^{-1}

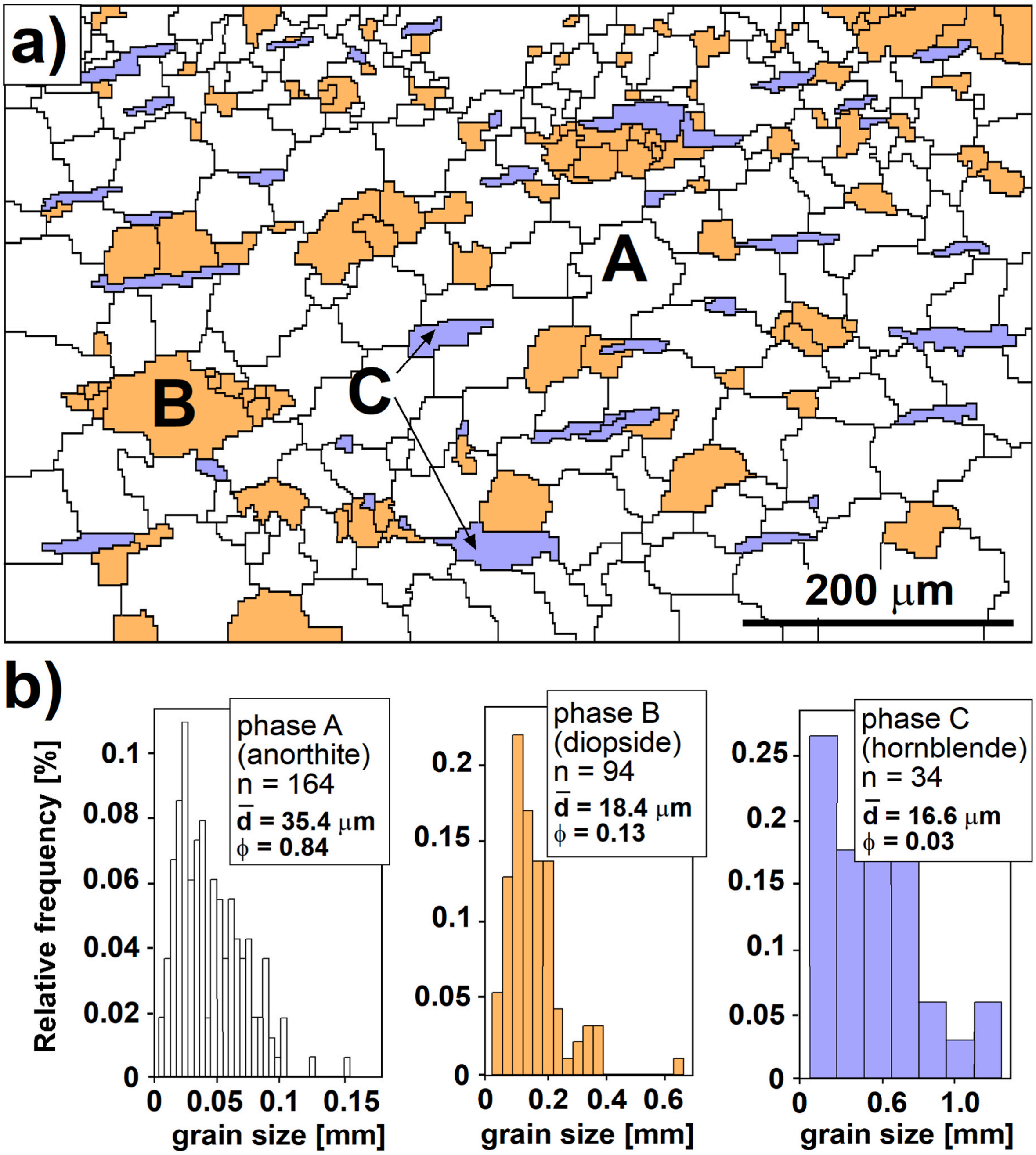

Fig. 2. Experimental setup of the model mylonite: a) microstructural map showing the distribution of the various mineral phases used in the simulation A (anorthite), B (diopside) and C (hornblende), b) grain size distribution of the various minerals based on n grains; φ = volume proportion, $\overline{d}$ = median diameter of the area-equivalent circle.

and peak strain rate of about $1 \times 10^{-11.7}$ s^{-1} localized in the hornblende crystals (Fig. 3g). At constant temperature, the average strain rate increases by about 4 orders of magnitude and reaches $1 \times 10^{-11.1}$ s^{-1} assuming a uniform stress of 10 MPa. Peak strain rates, close to $1 \times 10^{-7.6}$ s^{-1} are still mostly concentrated within hornblende crystals, although diopside records strain rates slightly higher than anorthite (Fig. 3h). Finally, at 100 MPa, the average strain rate calculated from Eq. (13) is $1 \times 10^{-9.0}$ s^{-1}, whereas deformation is strongly concentrated into hornblende reaching values of about $1 \times 10^{-4.6}$ s^{-1} (Fig. 3i). The strain rate dependence on stress is similar at lower temperature of 750 °C, as hornblende is still the phase that concentrates deformation. Yet, the increase of strain rate for increasing stress is less rapid from about $1 \times 10^{-15.6}$ s^{-1} at 1 MPa to $1 \times 10^{-9.6}$ s^{-1} at 100 MPa (Fig. 3i-l).

3.1.2. *Deformation mechanisms*

The pattern of deformation mechanisms that emerges from one or the other mechanical boundary condition provides useful information that could be used to test the validity of rheological models in relation to the mylonite microstructure (i.e., Bell and Etheridge, 1976; Hirth and Tullis, 1992; Campbell and Menegon 2019; Casini et al., 2021). In the iso-strain rate experiments, for instance, the dominant deformation mechanisms are grain boundary sliding and diffusion creep, being dislocation creep active only for very high strain rates in hornblende crystals (Fig. 4a–b). Overall, high temperature and lower strain rates promote diffusion creep (Fig. 4c,f), which is consistent with the observation of Newtonian creep in HT deformation experiments of mono-mineralic anorthite aggregates (Gomez Barreiro et al., 2007; Mehl and Hirth, 2008; Rybacki et al., 2010) and composite mixtures of anorthite

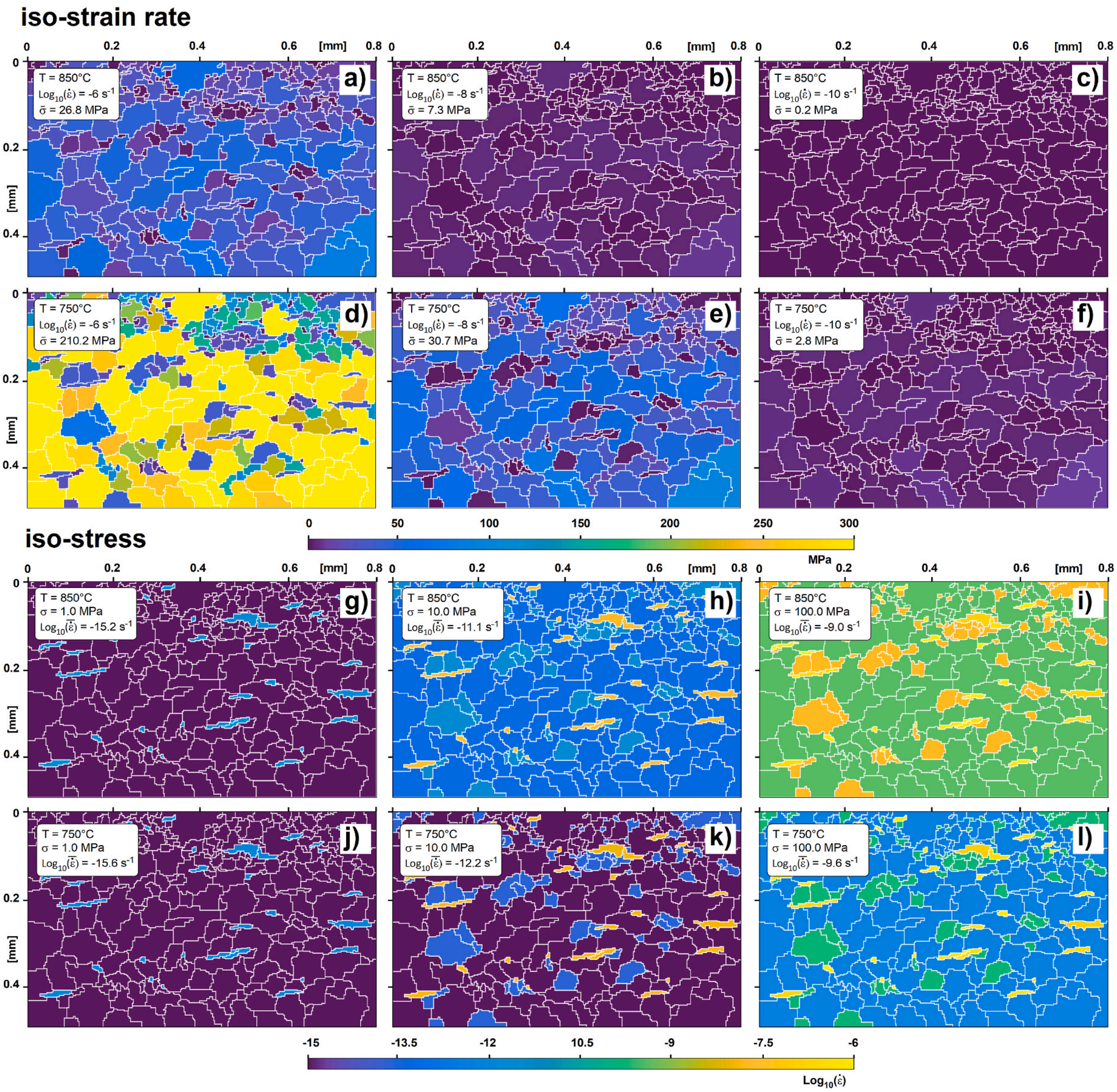

Fig. 3. Results of rheological modelling of the model mylonite microstructure: a-c) stress distribution for uniform strain rate of $1 \times 10^{-6}\ s^1$ to $1 \times 10^{-10}\ s^1$ (iso-strain rate condition) and temperature of 850 °C; d-f) stress distribution for uniform strain rate of $1 \times 10^{-6}\ s^1$ to $1 \times 10^{-10}\ s^1$ (iso-strain rate condition) and temperature of 750 °C; g-i) strain rate distribution for uniform stress between 1 and 100 MPa (iso-stress condition) and 850 °C; j-l) strain rate distribution for uniform stress between 1 and 100 MPa (iso-stress condition) and 750 °C. The symbols $\bar{\sigma}$ and $log_{10}\overline{(\dot{\varepsilon})}$ denote the mean stress and mean strain rate, respectively, calculated from Eq. (11).

and diopside (Dimanov and Dresen, 2005; Dimanov et al., 1999; 2003; 2007). Under the assumption of iso-stress condition, the pattern of deformation mechanisms does not change from the experiments at 850 °C and those at 750 °C (Fig. 4g–i). Regardless of temperature, dislocation creep is expected to be the dominant deformation mechanism in the range 1–100 MPa of bulk stress, yet grain boundary sliding and diffusion creep activate at higher stress (Fig. 4h and i).

4. Analysis of natural mylonites

For the purpose of demonstration, we analysed three different mylonite samples deformed within crustal shear zones under increasing metamorphic conditions, from around the brittle-ductile transition up to the lower amphibolite facies (Casini and Funedda, 2014; Katori et al., 2021; Zhang et al., 2022). All samples have available robust paleopiezometric analysis based on classical grain size-stress calibrations of the form of Eq. (12), crystallographic preferred orientation (CPO) data, microstructural analysis and the pressure-temperature conditions of deformation. For each mylonite sample we performed first a suite of 0th dimensional simulations assuming either an iso-stress or iso-strain rate mechanical constraint (Fig. 5). In these models, the bulk flow law parameters of mylonite were derived using the arithmetic average or the thermodynamic mixing rule (Hobbs et al., 2019). Then, based on the outcomes of 0th dimensional models, we simulate the distribution of stress, strain rate and deformation mechanisms in mylonites through a set of 2D models which solve Eq. (1), or its equivalent formulation in terms of stress, using as local (grain-scale) deformation mechanism the one that minimizes stress or strain rate (Figs. 6–8).

4.1. Baccu Locci Shear Zone mylonite

The Baccu Locci Shear Zone is a steeply-dipping, reverse shear zone formed in the Variscan external nappes of Sardinia during the Carboniferous phase of crustal shortening (Conti et al., 1998; 1999; 2001). Microstructural analysis and thermobarometry indicate that the pressure-temperature conditions of deformation were about 350–380 °C and 0.35–0.4 GPa, respectively. Independent geological constraints based on the timing of shear zone activity suggest that deformation

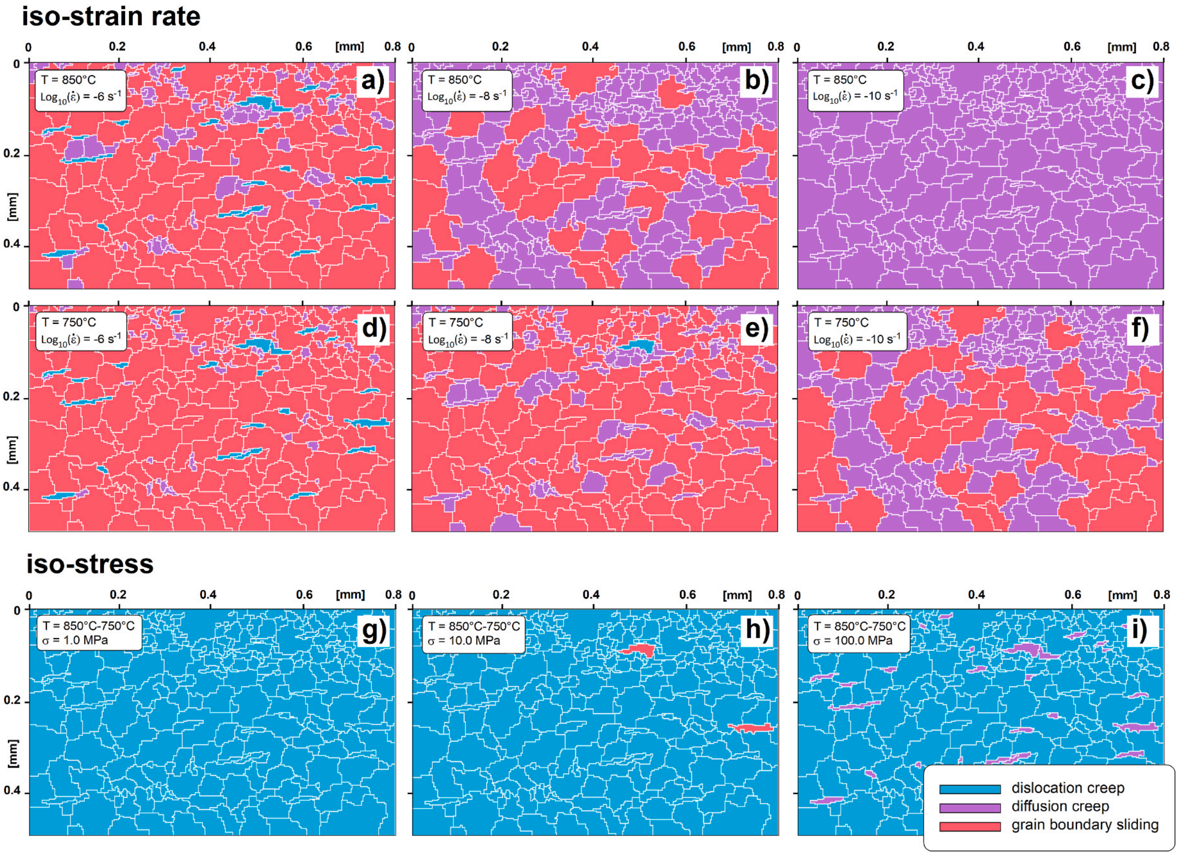

Fig. 4. Distribution of deformation mechanisms in the model mylonite for the experiments shown in Fig. 3: a-c) iso-strain rate experiments at 850 °C; d-f) iso-strain rate experiments at 750 °C; g-i) iso-stress experiments. Note that in the range of 1–100 MPa stress, deformation mechanisms do not change for temperature of either 850 °C or 750 °C.

occurred at minimum strain rates of about 1×10^{-13} s^{-1} and likely not exceeding 1×10^{-11} s^{-1} (i.e., Casini et al., 2010; Casini and Funedda, 2014). In this study, we model the rheology of sample Af116 (Fig. 6a–b), which corresponds to a medium-strained mylonite of the central part of the shear zone (i.e., Casini and Funedda, 2014). Sample AF116 derive from an Ordovician rhyolite emplaced within a continental volcanic arc (i.e., Cocco and Funedda, 2019; Cocco et al., 2018; 2023; Loi et al., 2023) and consists largely of quartz (82 vol%), muscovite (17 vol%) and K-feldspar (1 vol%). The microstructure is characterized by large quartz porphyroclasts mantled by fine-grained recrystallized tails of quartz and muscovite forming incipient ribbons (Fig. 6a). The microstructure suggests that deformation is mainly accommodated by dislocation creep involving subgrain rotation in quartz porphyroclasts and grain-boundary sliding in mica-rich fine grained domains, eventually combined with pressure solution creep (Casini and Funedda, 2014). The median grain size of quartz, based on 3550 grains, is about 14 μm, whereas that of feldspar (16 grains) and muscovite (266 grains) are 28 μm and 16 μm, respectively (Fig. 6b). Quartz paleopiezometry provided stress values ranging from about 40 to 90 MPa depending on the calibration used (Casini and Funedda 2014). Assuming an iso-stress mechanical condition, the strain rates determined by independent geological constraints can be fit for stress values between about 12 and 50 MPa using the arithmetic average of the flow law parameters (Fig. 5a). Quite higher stress values, ranging from about 54 to >200 MPa (Fig. 5a), are obtained using the thermodynamic mixing rule (Hobbs et al., 2019). On the other hand, under an iso-strain rate condition, both mixing models match the stress values determined from quartz recrystallized grain size paleopiezometry only assuming high strain rates >1 $\times 10^{-10.7}$ s^{-1} (Fig. 5b). The first 2D rheological model assumes an iso-strain rate mechanical constraint and was run at 370 °C. We start the simulation using a maximum bulk strain rate of 1×10^{-10} s^{-1}, which has been decreased stepwise until reaching peak stress close to 590 MPa and an average stress of 53.4 MPa, which is close to the median stress value obtained from quartz paleopiezometry. These stress values correspond to an average strain rate of about $1 \times 10^{-11.2}$ s^{-1} (Fig. 6c). At these conditions, the largest quartz and muscovite porphyroclasts accommodate dislocation creep, whereas the dominant deformation mechanisms in the fine-grained quartz-muscovite matrix are grain boundary sliding and diffusion creep, which corresponds to pressure solution creep given the low temperature of deformation (Fig. 6d). The last rheological model uses an iso-stress condition and assumes an average stress of 70 MPa, close to the median value estimated from quartz paleopiezometry. At these conditions, the average strain rate is about $1 \times 10^{-12.3}$ s^{-1} with peak strain rate of about $1 \times 10^{-8.3}$ s^{-1} localized in the smaller muscovite crystals (Fig. 6e). In this second model, the large quartz porphyroclasts, feldspar, and most of the muscovite crystals deform by low-temperature diffusion creep whereas the quartz-rich fine-grained matrix accommodates dislocation creep (Fig. 6f).

4.2. Median Tectonic Line quartzite-mylonite

The Median Tectonic Line exposed in SW Japan is a major crustal-scale shear zone separating the LP-HT Ryoke metamorphic belt from the HP-LT Sambagawa terrane (i.e., Ichikawa 1980). It is tectonically active since the Cretaceous with dominant strike-slip kinematics alternating to extensional phases (i.e., Fukunari and Wallis, 2007; Shigematsu et al., 2017; Kubota et al., 2020). We evaluate the distribution of deformation mechanisms and differential stress in one sample of relatively HT mylonite (Fig. 7a) collected close to the Median Tectonic Line in the Kii peninsula, SW Japan (sample S30; Katori et al., 2021). The

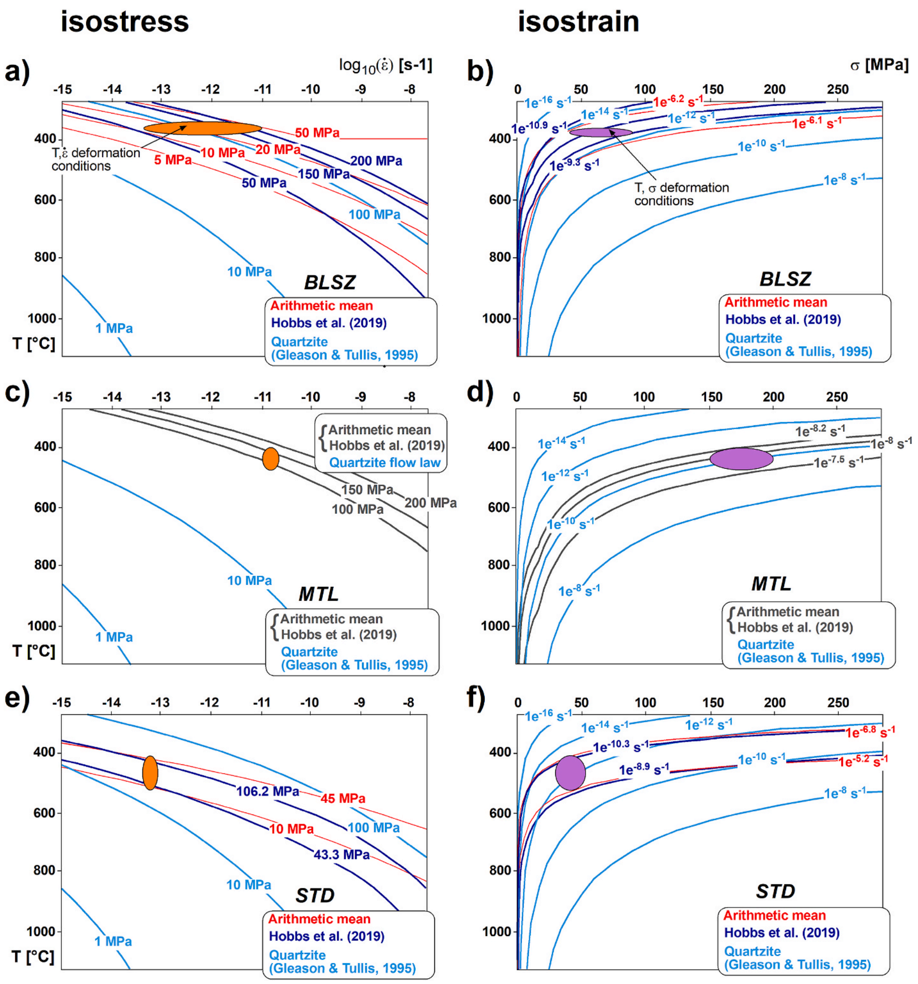

Fig. 5. 0^{th} dimensional rheological models of natural mylonite obtained using either an iso-stress mechanical constraint (panels a,c,e) or iso-strain rate condition (panels b,d,f). In all diagrams, the red curves mark the composite strength calculated by arithmetic averaging the flow law parameters of its constituent phases. The dark blue curves denote the composite strength calculated based on the Hobbs et al. (2019) logarithmic mixing rule. The light blue curves are calculated from the dislocation creep flow law of pure quartzite (Gleason and Tullis, 1995). The temperature and strain rates extrapolated independent geological constraints are shown as orange ellipses in the iso-stress experiments, whereas temperature and stress derived from recrystallized grain size paleopiezometry are shown as violet ellipses in the iso-strain rate experiments, respectively. BLSZ = Baccu Locci Shear Zone mylonite (Casini and Funedda, 2014), MTL = Median Tectonic Line mylonite (Katori et al., 2021), STD = South Tibetan Detachment mylonite (Zhang et al., 2022). (For interpretation of the references to colour in this figure legend, the reader is referred to the Web version of this article.)

analysed mylonite is monomineralic (quartz = 100 vol %) and consists of large, >100 μm-wide, highly stretched quartz grains showing diffuse evidence of lattice strain such as sub-grains and Dauphiné twinning, and recrystallized domains composed of much smaller quartz grains. The microstructure of this monomineralic quartz-mylonite indicates that deformation is accommodated by a combination of subgrain rotation and grain boundary sliding (Katori et al., 2021). The median grain size of the fine-grained recrystallized domains, based on 177 measures, is about 11.2 μm (Fig. 7b). Chlorite thermometry combined with two-feldspars thermometry applied to polymineralic samples collected close to sample S30 in an equivalent structural position indicate that deformation temperature ranges between about 400 and 480 °C (Katori et al., 2021). It should be noted that sample S30 is off the range of applicability of recrystallized grain size paleopiezometry, as the rock did not attain microstructural steady state possibly due to short-lived deformation events (Katori et al., 2021). Yet, these authors suggest that HT mylonites close to the median Tectonic Line might have recorded high differential stress up to 200 MPa, as the grain size of the small, recrystallized domains is like the mean grain size of highly strained low temperature mylonites deformed at the brittle-plastic transition (Katori et al., 2021). Based on the transition between deformation mechanisms and the thickness of high-strain zones, several authors infer that deformation in the high-temperature segment of the Median Tectonic Line involve strain rates around 1×10^{-11} s^{-1} (Okudaira and Shigematsu, 2012). Under an iso-stress condition, these strain rates require stress values of about 100–120 MPa at about 440 °C. In this mylonite there is no difference between the arithmetic average and the thermodynamic mixing rule as the rock is nominally monomineralic (Fig. 5c). Assuming an iso-strain rate condition, both mixing models return strain rates between $1 \times 10^{-7.5}$ s^{-1} and $1 \times 10^{-8.2}$ s^{-1} (Fig. 5d). The 2D rheological models shown in Fig. 7c–f assume a deformation temperature of 440 °C, which is representative for HT mylonites in the Kii peninsula (Katori et al., 2021). In the first model we assume an iso-strain mechanical condition. Based on this assumption, we increase the strain rate from an initial value of 1×10^{-13} s^{-1} by stepwise increments until the mean stress calculated from Eq. (11) approaches 99.2 MPa, a value close to the lower limit of stress deduced from paleopiezometry in adjacent mylonites that attained steady-state microstructure (Katori et al., 2021). At these conditions, peak stress within the smallest recrystallized quartz grains reaches about 180 MPa (Fig. 7c). These stress values correspond to 1×10^{-9} s^{-1} strain rate, thus one to two orders of magnitude higher than the strain rates estimated for the high-temperature segment of the Median

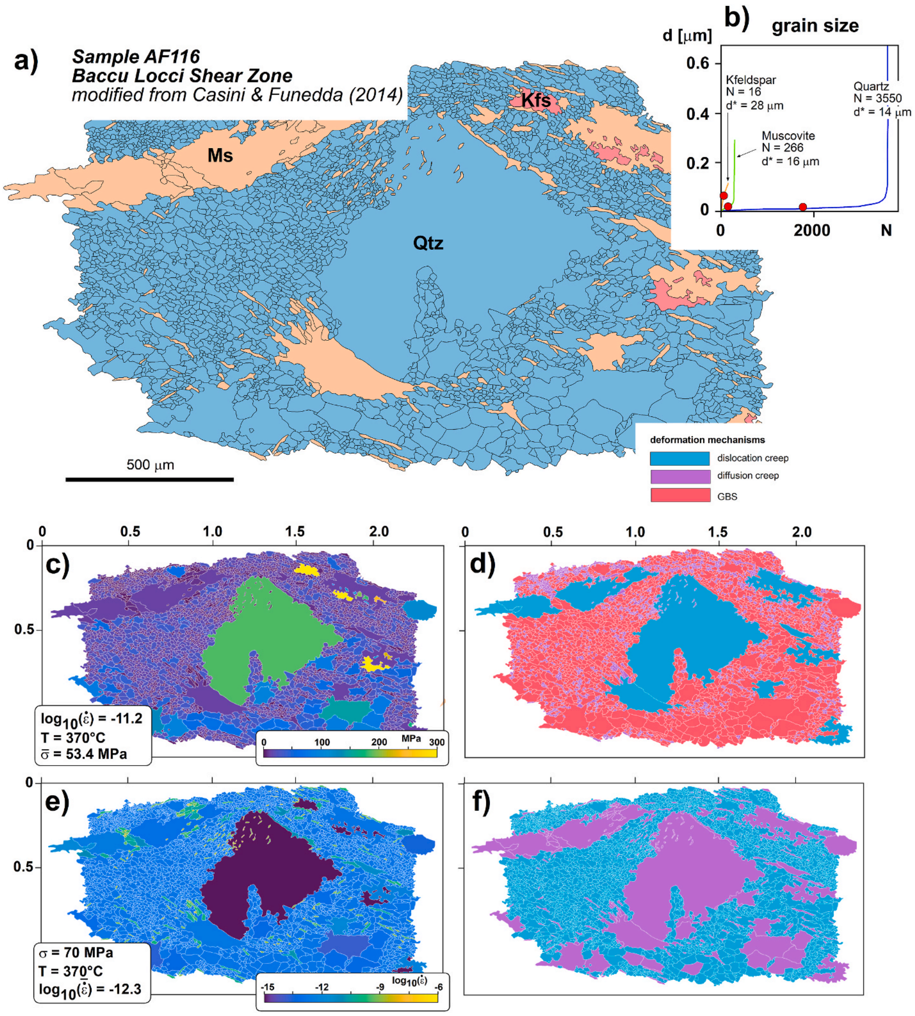

Fig. 6. 2D rheological models of sample AF116 from the BLSZ (Casini and Funedda, 2014): a) microstructural phase map showing the distribution of quartz (Qtz), K-feldspar (Kfs) and muscovite (Ms), as well as the grain topology; b) grain size distribution, average grain size (d*) and number of grains (N) of the various phases; c) stress pattern corresponding to a uniform strain rate of 1 × 10^{-10} s^{1} (iso-strain rate condition) and a temperature of 370 °C. The symbol $\overline{\sigma}$ denotes the average stress calculated from Eq. (11); d) distribution of deformation mechanisms for the experiment shown in c; e) strain rate pattern corresponding to a uniform stress of 70 MPa (iso-stress condition) and a temperature of 370 °C. The symbol $log_{10}\overline{(\dot{\varepsilon})}$ denotes the average strain rate calculated from Eq. (11); f) distribution of deformation mechanisms for the experiment shown in e.

Tectonic Line and other equivalent deep seismogenic faults (i.e., Sibson 1982; Hacker et al., 1992; Okudaira and Shigematsu, 2012). Under these conditions, the stable deformation mechanisms are grain boundary sliding in most of the mylonite and diffusion creep in the smallest recrystallized quartz grains (Fig. 7d). The second model (Fig. 7e) assumes an iso-stress mechanical condition. We start using a uniform stress of 180 MPa, which corresponds to an average strain rate of 1 × $10^{-10.2}$ s^{-1} and somewhat higher peak strain rates of about 1 × $10^{-9.9}$ s^{1}. Successively, we reduce the stress value until the average strain rate approaches a mean value of 1 × $10^{-10.9}$ s^{-1}, consistent with the lower bound of bulk strain rate estimates based on independent geological constraints (Okudaira and Shigematsu, 2012; Katori et al., 2021). The target strain rate requires about 110 MPa (Fig. 7e). At these conditions, dislocation creep is the active deformation mechanism in the recrystallized domains (Fig. 7f).

4.3. South Tibetan Detachment mylonite

The South Tibetan Detachment (STD) is a major ductile shear zone exposed in the western-central part of the Himalayan chain. According to recent thermo-mechanical geological models (i.e., Beaumont et al., 2006; Mukherjee, 2012), the STD in cooperation with the structurally deeper Main Central Thrust accommodated tectonic extrusion of the Greater Himalayan Sequence from latest Oligocene until late Miocene (i.e., Searle et al., 1997; Dong et al., 2020). We evaluate the distribution of stress, strain rate and deformation mechanisms in one quartz-feldspatic mylonite sample, YD-056 (Fig. 8a), collected in the ductile segment of the STD. The sample consists of K-feldspar (47 vol%), quartz (27 vol%), and plagioclase (26 vol%). A comprehensive microstructural study including rheological analysis, EBSD-based crystallographic preferred orientation, and quartz recrystallized grain size paleopiezometry is provided in a recent paper by Zhang et al. (2022). The analysed mylonite is composite and consists of large, >1 mm-long, partly recrystallized K-feldspar porphyroclasts wrapped by finer grained layers of quartz and plagioclase (Fig. 8a). The microstructure indicates that deformation is accommodated by a combination of subgrain rotation-recrystallization and grain boundary migration, which implies dislocation creep and grain boundary-controlled diffusion creep (Zhang et al., 2022). The median grain size of the recrystallized quartz, plagioclase and K-feldspar aggregates is nearly equant with values of about 64, 67 and 58 µm, respectively (Fig. 8b). Two-feldspars thermometry indicates that sample YD-056 deformed at about 470 °C (Zhang et al., 2022). The same authors suggest differential stress between about 30 and 35 MPa and relatively low strain rates between 1.3 × 10^{-13} s^{-1} and 3.3 × 10^{-13} s^{-1}.

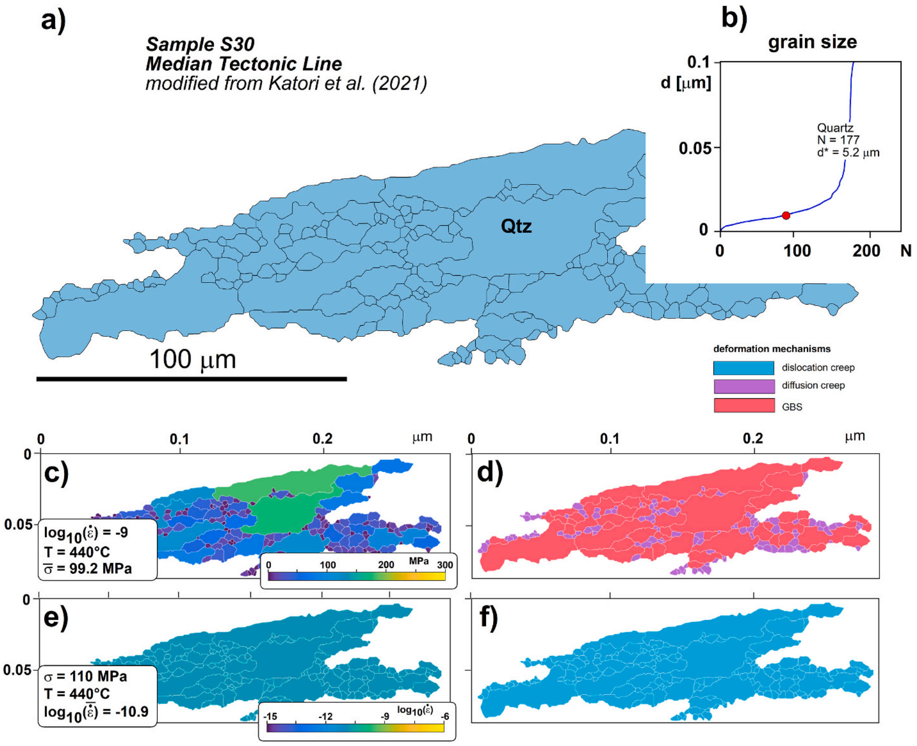

Fig. 7. 2D rheological models of sample S30 from the MTL (Katori et al., 2021): a) microstructural phase map; b) grain size distribution, average grain size (d*) and number of recrystallized quartz grains (N); c) stress pattern corresponding to a uniform strain rate of 1×10^{-9} s^{1} (iso-strain rate condition) and a temperature of 440 °C; d) distribution of deformation mechanisms for the experiment shown in c; e) strain rate pattern corresponding to a uniform stress of 110 MPa (iso-stress condition) and a temperature of 440 °C; f) distribution of deformation mechanisms for the experiment shown in e. The symbols used to denote the average stress and strain rate calculated from Eq. (11) are the same as in Fig. 6.

Using an iso-stress mechanical condition, the geological strain rates and temperatures can be reproduced by arithmetic averaging the flow law parameters for stress values between about 10 and 45 MPa (Fig. 5e). Again, higher stress values ranging from about 43.3 to >106.2 MPa (Fig. 5e) are obtained using the thermodynamic mixing rule (Hobbs et al., 2019). The iso-strain rate condition provides lower strain rate values between $1.0 \times 10^{-10.3}$ s^{-1} and $1.0 \times 10^{-8.9}$ s^{-1} using the thermodynamic mixing rule (Hobbs et al., 2019), whereas higher values between $1.0 \times 10^{-6.8}$ s^{-1} and $1.0 \times 10^{-5.2}$ s^{-1} correspond to the arithmetic (Fig. 5f). In the 2D models we use firstly an iso-stress mechanical condition assuming the microstructure of sample YD-056 correspond to a uniform stress of about 33 MPa, consistent with that calculated from the quartz recrystallized grain size paleopiezometry (i.e., Zhang et al., 2022). Then, we repeat the simulation prescribing a uniform strain rate of 1×10^{-12} s^{-1} that corresponds to the maximum time-averaged strain rates calculated for the South Tibetan Detachment based on the shear zone width and the available geochronological constraints (i.e., Cottle et al., 2007; Gong et al., 2012; Zhang et al., 2022). The first model shows that 33 MPa uniform stress corresponds to marked partitioning of deformation, with peak strain rates of $1 \times 10^{-12.2}$ s^{-1} in the fine-grained quartz layers and much lower strain rate of 1×10^{-15} s^{-1} to 1×10^{-17} s^{-1} in the large K-feldspar porphyroclasts and plagioclase aggregates (Fig. 8c). The bulk strain rate calculated from Eq. (11) is $1 \times 10^{-13.4}$ s^{-1}. Deformation is mainly accommodated by dislocation creep, except in the finer grained domains of the quartz ribbons where diffusion creep become effective (Fig. 8d). The second model shows that for uniform strain rate of 1×10^{-12} s^{-1}, peak stress of about 25 MPa are attained in the fine-grained quartz layers, whereas plagioclase and K-feldspar record lower stress generally below 5 MPa (Fig. 8e). The bulk stress calculated from Eq. (11) is about 3 MPa due to the much larger molar volume of plagioclase and K-feldspar. Under the conditions of the second model, deformation is accommodated by grain boundary sliding and diffusion creep, being this latter concentrated in the fine-grained quartz-rich layers (Fig. 8f).

5. Discussion

The results obtained from the analysis of theoretical microstructures and natural mylonite samples are briefly discussed, mainly focusing on the micro-mechanical processes that yield to grain-scale partitioning of stress and strain rate in mylonites. The potential consequences and limitations for the applicability of grain size piezometers will be also discussed in the final section of the paper.

5.1. Effect of the mixing rule

Overall, the results of rheological modelling indicate that the flow of mylonite is influenced by its composition and by topological aspects, such as grain size and spatial distribution of the various mineral phases. A clear tendency already emerges in monomineralic rocks characterized by large variation of the grain size, such as sample S30 from the Median Tectonic Line, as most rock-forming minerals switch from power law to linear Newtonian creep once the grain size decreases to a given threshold value (i.e., Gomez Barreiro et al., 2007; Précigout et al., 2007; Mehl and Hirth, 2008; Platt and Behr, 2011a). This implies that a given mean bulk stress requires lower strain rates under the assumption of uniform stress compared to the experiments assuming uniform strain rate (i.e., Fig. 7c,e). Composites take this behaviour to the extremes because of the material-dependent flow law parameters of different mineral phases are commonly characterized by very large variations, up to several orders of magnitude (i.e., Gleason and Tullis, 1995; Bruijn and Skemer, 2014). This implies that the bulk strength of mylonite can substantially decrease for even relatively low proportions of weak mineral phases such as calcite, muscovite or biotite (Mares and

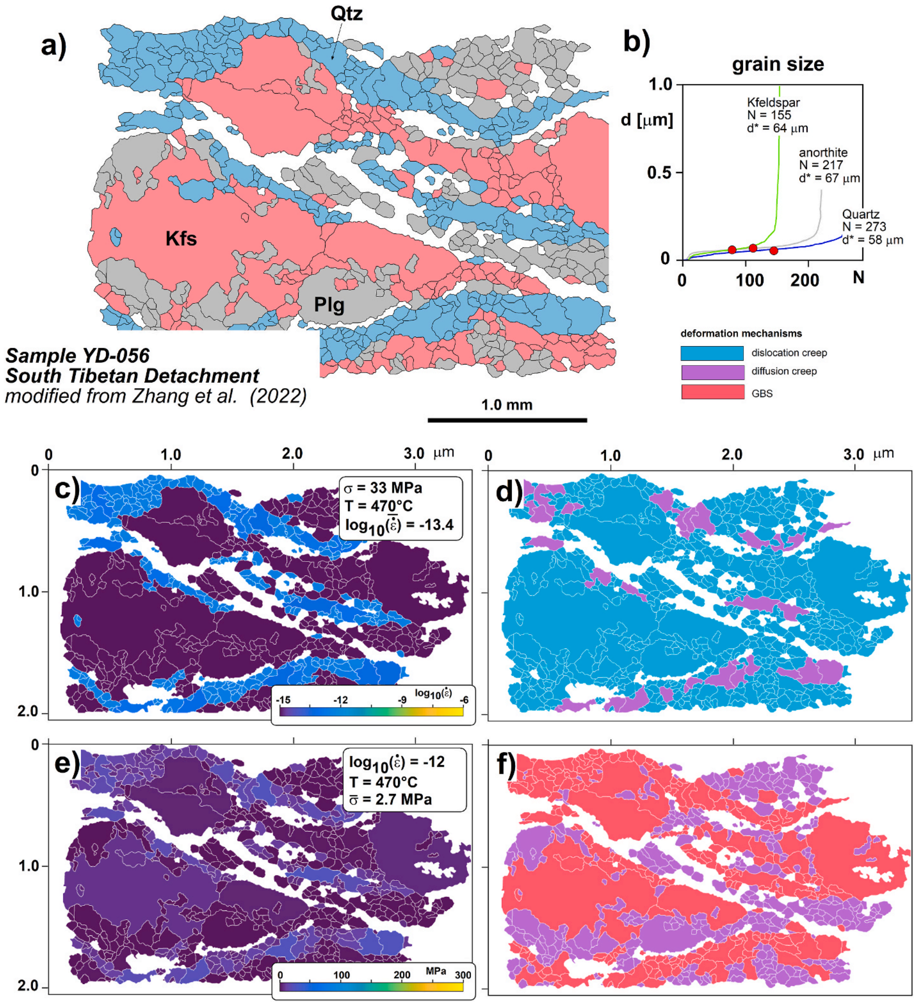

Fig. 8. 2D rheological models of sample YD-056 from the STD (Zhang et al., 2022): a) microstructural phase map; b) grain size distribution, average grain size (d*) and number of grains (N) of quartz (Qtz), K-feldspar (Kfs) and anorthite (Plg); c) strain rate pattern corresponding to a uniform stress of 33 MPa (iso-stress condition) and a temperature of 470 °C; d) distribution of deformation mechanisms for the experiment shown in c; e) stress pattern corresponding to a uniform strain rate of 1 × 10^{-12} s^{1} (iso-strain rate condition) and a temperature of 470 °C; f) distribution of deformation mechanisms for the experiment shown in e. The symbols used to denote the average stress and strain rate calculated from Eq. (11) are the same as in Fig. 6.

Kronemberg, 1993; Handy 1994; Rutter, 1995; Handy et al., 1999). However, 0^{th} dimensional models show that the effective bulk strength of composite mylonites is subjected to large uncertainties which largely depend on the choice of the mixing rule (i.e., Handy et al., 1999; Ji et al., 2003; Huet et al., 2014; Hobbs et al., 2019). Sample AF116 from the Baccu Locci Shear Zone, for instance, is a nearly bi-mineralic mylonite composed of quartz ($\sim$80 vol%) and muscovite ($\sim$20 vol%). Muscovite is expected to be much weaker than quartz under the temperature, pressure, and strain rate conditions of deformation (i.e., Mares and Kronemberg, 1993). However, its impact on the bulk rheology of mylonite is mostly detectable using one of the mixing rules that use volume proportions to weight the relative contribution of each phase. This behaviour is particularly obvious using the harmonic average, as the contribution of each phase to the bulk strength of mylonite is inversely proportional to the strength of that phase. However, also the arithmetic, geometric or Minimized Power Geometric average models show a similar tendency. On the other hand, the thermodynamic mixing model predicts strength profiles nearly overlapping those of pure quartzite because of using molar proportions instead of volume proportions greatly enhances the contribution of minerals with smaller molar volume such as quartz. Under the assumption of an iso-stress condition the arithmetic average underestimates the strength of the composite, thus stress calculated from quartz recrystallized grain size paleopiezometry could be match only assuming very high strain rates larger than 1 × 10^{-11} s^{-1}, which is above the range of geologically permissible strain rates (Fig. 5a). Conversely, the thermodynamic mixing model fit well the paleopiezometric data for strain rates between 1 × 10^{-13} s^{-1} and 1 × 10^{-12} s^{-1}, in good agreement with the limits imposed by independent regional geological constraints (Conti et al., 1998; 1999; 2001; Casini et al., 2021; Casini and Funedda, 2014). The reason for this discrepancy is quite straightforward, as weighting the flow law parameters of the composite by the molar volume proportions of its constituent phases rather than by their volume proportions amplifies the influence of minerals with smaller molar volume (Robie and Bethke 1962; Hobbs et al., 2019). The influence of using one mixing model in place of another become less important whenever the various phases have similar molar volume, such as in sample YD-056 from the South Tibetan Detachment (Zhang et al., 2022). In this sample, K-feldspar and plagioclase are the stronger phases, while quartz is expected to be relatively weaker at the inferred conditions of deformation. The differences between the strength profiles calculated from arithmetic average and the thermodynamic mixing rule are still detectable, though largely reduced possibly because of the quite similar volume proportion of the various phases, and the relatively low variability of the flow-law parameters. Shear numerical experiments compared with mechanical data show, in fact, that the rheology of composite mylonite is strongly sensitive on the proportion between weak and strong phases, being the variability maximum for larger viscosity contrast and for strongly uneven phase proportions (Rast and Ruh, 2021).

5.2. Average stress and deformation partitioning in composite mylonites

The 2D maps show the grain scale distribution of stress, strain rate and deformation mechanism offering the opportunity to evaluate the conditions that promote deformation partitioning in mylonite, as well as to test the effectiveness of either the iso-strain rate or iso-stress mechanical constraint (Voigt, 1928; Reuss, 1929). 2D maps, in fact, allow to compare the observed grain-scale deformation mechanisms and those predicted assuming one or the other mechanical constraint. This type of application is best explained using composite mylonite AF116 from the Baccu Locci Shear Zone as an example. Based on microstructural observation and textural analysis, the sample is expected to have deformed by a combination of dislocation creep and pressure solution creep (Casini and Funedda, 2014). Under the assumption of uniform stress, these deformation mechanisms are effective for average stress matching that derived from quartz paleopiezometry, and the mylonite apparently dissipates geologically admissible strain rates of about $1 \times 10^{-12.3}$ s^{-1} (Fig. 6f). Deformation was weakly partitioned in this model, as the large quartz porphyroclast remains mostly undeformed recording very low strain rates below 1×10^{-16} s^{-1}, whereas the fine-grained matrix flows at much higher strain rates without any noticeable concentration of deformation (Fig. 6e). This observation is suggestive of near steady-state condition, which is consistent with the observed strain gradient and the microstructural transformation recorded from the shear zone boundary toward the zone of high strain (Casini et al., 2021; Casini and Funedda, 2014). On the contrary, using an iso-strain rate condition, deformation would have been accommodated by grain boundary sliding assisted by diffusion creep, enhancing extreme stress partitioning between muscovite, quartz, and feldspar (Fig. 6d). Thus, by combining microstructural observation, geological arguments and the 2D rheological models, we argue that deformation occurred close to an iso-stress mechanical condition, in good agreement with the theoretical behaviour of mature crustal-scale shear zones (i.e., Platt and Behr, 2011b). A similar analysis conducted on sample YD-056 from the South Tibetan Detachment (Zhang et al., 2022) confirms that nearly iso-stress conditions would be required, also in this case, to fit the deformation mechanisms and strain rates inferred from microstructural observation and independent regional geological constraints. Dislocation creep in the K-feldspar boudins and combined diffusion plus dislocation creep in the quartz layers, in fact, can be obtained for a uniform stress of 33 MPa, consistent with the estimate based on quartz paleopiezometry (Fig. 8c and d). Under this assumption, deformation is extremely partitioned yielding to high, though realistic, strain rates close to 1×10^{-11} s^{-1} within quartz layers, whereas K-feldspar boudins remain nominally undeformed (Fig. 8e and f).

5.3. Applicability of recrystallized grain size piezometers

Stress is an intensive physical parameter. This implies that calculating the average stress value of a composite mylonite with heterogeneous grain size does not require to account for the total mass of grains characterized by a given stress value. Therefore, a simple statistical model such as the geometric or arithmetic average could be used to find the central value if stress had to be measured directly. Paleopiezometric calibrations of the form of Eq. (12), sometimes including a temperature-dependent formulation of the term θ (i.e., De Bresser et al., 1998; Ter Heege et al., 2004b; Shimizu, 2008), assume that the recrystallized grain size of an aggregate is proportional to the applied shear stress. The foundations of this assumption derive from the theory of dynamic recrystallization, which involves on the one side grain size reduction by sub-grain rotation and bulging, and, on the other side, grain growth accommodated by grain boundary diffusion (i.e., Poirier, 1985; Humphreys and Hatherly, 1995; Shimizu, 2008). Both type of processes reflects stress-driven changes of the strain energy. Grain size reduction, in fact, is generally viewed as a microstructural adjustment necessary to minimize the component of strain energy due to increases of dislocation density related to flow stress (i.e., Poirier, 1985; De Bresser et al., 1998; Shimizu, 2008; Platt and Behr, 2011a). On the other hand, grain growth is a complementary mechanism that reduce the number of recrystallized grains preventing the rocks to accumulate too high values of grain surface energy (Atkinson, 1988). According to this model, the equilibrium grain size should reflect the balance between stress-driven grain-size reduction and grain growth, which is a thermally activated process also dependent on stress (De Bresser et al., 1998). Regardless of possible complications due to still uncertain aspects of the microphysical model such as the complex interactions between different deformation mechanisms and different phases (i.e., Ter Heege et al., 2004; Austin and Evans, 2007; Hobbs et al., 2019), it should be noted that the grain size of mylonite provides a snapshot of the strain energy function, and not stress. Such observation raises fundamental concerns about the general applicability of empirically calibrated recrystallized grain size piezometers, as the strain energy is an extensive thermodynamic variable, thus it must obey the classical Boltzmann-Gibbs statistics. This implies that the average stress of any polycrystalline aggregate, either monomineralic or composite, should be calculated by weighting single grain stress values for their respective mass, and not using a descriptive statistic approach such as commonly used in paleopiezometric studies (i.e., Casini and Funedda, 2014; van der Werf et al., 2017; Melosh et al., 2018; Casini and Funedda, 2014; Katori et al., 2021; Zhang et al., 2022). 2D rheological models using the iso-strain rate mechanical constraint provide a way around these limitations, as the average stress of a composite mylonite can be calculated based on thermodynamically consistent principles from Eq. (11). In general, the average stress calculated from 2D iso-strain rate models fits the paleopiezometric results. Yet, the mean stress predicted by Eq. (11) is systematically lower than that derived from empirically calibrated piezometers, and the difference between both estimates increases as the molar proportions of mylonite mineral phases become nearly equal. As an example, sample S30 from the Median Tectonic Line (Katori et al., 2021) is monomineralic and corresponds to an average stress of 110 MPa for geologically realistic strain rates, perfectly overlapping the value obtained from the recrystallized grain size of quartz (i.e., Katori et al., 2021). The fit between quartz paleopiezometry and the iso-strain rate model slightly decreases by 10–20 out of 60–90 MPa in sample AF116 (Baccu Locci Shear Zone, Casini and Funedda, 2014), and become obviously divergent in the composite mylonite YD-056 (South Tibetan Detachment, Zhang et al., 2022), where the average stress predicted by the iso-strain rate model is one to two orders of magnitude lower than that calculated from paleopiezometry. The reason for these discrepancies is twofold. As repeatedly pointed by most authors, the mixing of different phases potentially stabilizes low grain sizes in the field dominated by grain boundary diffusion, yielding to an overestimation of the flow stress (Zener, 1951; De Bresser et al., 1998; Hobbs et al., 2019; Stipp et al., 2010). This effect is even amplified using the median grain of the various phases in place of their actual grain size distributions, as routinely done in paleopiezometric studies (i.e., Casini et al., 2021; Casini and Funedda, 2014; Ortolano et al., 2020; Katori et al., 2021; Zhang et al., 2022). Using the median grain size as a descriptor of some equilibrium microstructure, in fact, might artificially expand the volume of mylonite effectively deforming by the mechanism the piezometer is calibrated for. Because of most piezometric calibrations are derived for power law deformation dislocation creep, an overestimation of this latter mechanism at the expenses of linear or near-linear processes such as pressure solution, Coble creep or grain boundary sliding is expected to result in large overestimation of the flow stress.

5.4. Limitations and future development of the software

MYflow models the viscous flow of mylonite in a simplified way including only dislocation creep, diffusion creep along the grain boundaries (Coble creep), and grain boundary sliding (Lifschitz GBS). The first limitation comes from the formulation of dislocation creep, which explicitly neglect the effect of water fugacity. Recent experimental works on some common nominally anhydrous minerals such as quartz, olivine, diopside and plagioclase demonstrated that water generally decreases the strength of monomineralic aggregates deforming by dislocation creep (i.e., Rybacki et al., 2010; Dimanov et al., 2007; Karato et al., 1986; Tokle et al., 2019). This implies that MYflow probably overestimate the strength of low temperature mylonites in the dislocation creep regime. However, the effect of water on composite mylonite where different deformation processes are operating in different grain sizes of a particular mineral and/or in different minerals of various grain sizes is still largely unknown. It seems likely that diffusion creep might be enhanced by the presence of fluids as long as pressure-solution or Coble creep are concerned; however, diffusion can occur in a wide range of metamorphic conditions giving way to pressure-solution creep at low temperatures (i.e., Den Brok, 1996; Gratier et al., 2009; Casini and Funedda, 2014), or to Coble creep at higher temperature and nominally dry conditions consistent with lower crustal shear zones (Ji and Martignole, 1994) and Nabarro-Herring creep at even extreme conditions typical of the deep mantle (Greenough, 1958; Carrez et al., 2007). Thus, MYflow likely underestimates the effectiveness of diffusive processes in very low grade, fine-grained, mylonite deforming in the presence of fluids. In spite of these limitations, our simple and consistent formulation of the flow law approximates for several minerals and various deformation mechanisms.

Another major limitation is that grain size is the only topological aspect which is explicitly accounted for by Eq. (1). Although dislocation creep and grain-boundary diffusion creep are largely independent on the geometry and spatial density of the grain boundaries (i.e., Shimizu, 2008), grain boundary sliding most likely not. Superplasticity, in fact, usually requires the cooperation of one or more accommodation processes such as elastic lattice distortion, dislocation climb, diffusion or microstructural lubrication to maintain the mechanical compatibility between grains during flow (i.e., Lifschitz, 1963; Langdon and Mohamed, 1976; Casini et al., 2021). Yet, even small grains deforming at high stress and high temperature may still accommodate diffusion or dislocation creep if their geometry prevent the slide of grains past each other. This conclusion is supported by the frequency of straight grain boundaries and nearly equant sizes in the aggregates effectively deformed by grain boundary sliding (i.e., Langdon, 2006; Miranda et al., 2016; Casini et al., 2021).

The consequence of using such simplified topological model is that MYflow overestimates the effectiveness of grain boundary sliding in fine-grained mylonites. Despite these limitations, the experiments presented demonstrate that MYflow provides a good estimation of the general rheology of both monomineralic and composite mylonites deforming by multi-process viscous flow. However, implementing a revised formulation of Eq. (1) to include the effect of water fugacity and a full description of grain topology could further improve the results.

6. Conclusions

The applicability of the software MYflow has been demonstrated using three mylonite models representative of shear zones developed from the brittle-ductile transition zone to middle crustal conditions. The code has been further benchmarked by analysing three natural mylonite samples for which a full characterization including CPO or EBSD-based textural analysis, thermo-barometric data, grain size distribution and bulk stress or strain rate values derived from independent geological constraints were available. The software reproduces satisfactorily the grain-scale distribution of effective deformation mechanisms both in theoretical microstructures and natural mylonite samples. Besides simple 0th dimensional rheological modelling, the code provides a robust method to calculate the mean flow stress supported by mylonite. Differently to most empirically calibrated grain size piezometers, the method used for deriving the mean stress values obeys the law of statistical thermodynamics and can be applied, without limitations, also to rocks composed of two or more mineral phases and variable grain size distribution. Finally, 2D rheological modelling allow to easily test different mechanical boundary conditions and can be used to evaluate if mylonite microstructure approximates iso-stress or iso-strain rate mechanical condition.

Author statement

Leonardo Casini: Conceptualisation, Methodology, Software development, Validation, Formal analysis, Writing - Original Draft. Matteo Maino: Software development and debug, Validation, Investigation, Writing. Ludovico Manna: Conceptualisation, methodology. Antonio Funedda: Investigation, validation.

Declaration of competing interest

The authors declare no potential competing interest.

Data availability

the software and the data used for demonstration are available for download from the public repository GitHub.

MYflow (Original data) (github)

Acknowledgements

This work has been developed within the framework of the project e.INS- Ecosystem of Innovation for Next Generation Sardinia (cod. ECS 00000038) funded by the Italian Ministry for Research and Education (MUR) under the National Recovery and Resilience Plan (NRRP) - MISSION 4 COMPONENT 2, "From research to business" INVESTMENT 1.5, "Creation and strengthening of Ecosystems of innovation" and construction of "Territorial R&D Leaders".

Appendix A. Supplementary data

Supplementary data to this article can be found online at https://doi.org/10.1016/j.jsg.2023.105006.

References

Abramson, E.H., Brown, J.M., Slutsky, L.J., Zaug, J., 1997. The elastic constants of San Carlos olivine to 17 GPa. J. Geophys. Res. 102 (B6), 253–263.

Atkinson, H.V., 1988. Theories of normal grain growth in pure single-phase systems. Acta Metall. 36, 469–491.

Austin, N.J., Evans, B. Paleowattmeters: a scaling relation for dynamically recrystallized grain size. Geology, 35, 343-346.

Beaumont, C., Nguyen, M.H., Jamieson, R.A., Ellis, S., 2006. Crustal flow modes in large hot orogens. In: Law, R.D., Searle, M.P., Godin, L. (Eds.), Channel Flow, Ductile Extrusion and Exhumation in Continental Collision Zones, vol. 268. Geological Society, London, Special Publications, pp. 91–145.

Bell, T.H., Etheridge, M.A., 1976. The deformation and recrystallization of quartz in a mylonite zone, central Australia. Tectonophysics 32, 235–267.

Berthé, D., Choukroune, P., Jegouzo, P., 1979. Orthogneiss, mylonite and non-coaxial deformation of granites: the example of the South Armorican Shear Zone. J. Struct. Geol. 1, 31–42.

Brander, L., Svahnberg, H., Piazolo, S., 2011. Brittle-plastic deformation in initially dry rocks at fluid-present conditions: transient behaviour of feldspar at mid-crustal levels. Contrib. Mineral. Petrol. 163, 403–425.

Brodie, K.H., Rutter, E.H., 1987. Deep crustal extensional faulting in the Ivrea zone of northern Italy. Tectonophysics 140, 193–212.

Bruijn, R.H.C., Skemer, P., 2014. Grain-size sensitive rheology of orthopyroxene. Geophys. Res. Lett. 41, 4894–4903. https://doi.org/10.1002/2014GL060607.

Bürgmann, R., Dresen, G., 2008. Rheology of the lower crust and upper mantle: evidence from rock mechanics, geodesy, and field observations. Annu. Rev. Earth Planet Sci. 36, 531–567.

Byerlee, J., 1978. Friction of rocks. Pure Appl. Geophys. 116, 615–626. https://doi.org/10.1007/BF00876528.

Campbell, L., Menegon, L., 2019. Transient high strain rate during localized viscous creep in the dry lower continental crust (Lofoten, Norway). J. Geophys. Res. Solid Earth 124 (10), 260. https://doi.org/10.1029/2019JB018052, 240–10.

Carrez, P., Ferré, D., Patrick, C., 2007. Implications for plastic flow in the deep mantle from modelling dislocations in MgSiO3 minerals. Nature 446, 68–70.

Casini, L., Funedda, A., 2014. Potential of pressure solution for strain localization in the BaccuLocci shear zone (Sardinia, Italy). J. Struct. Geol. 66, 188–204. https://doi.org/10.1016/j.jsg.2014.05.016.

Casini, L., Funedda, A., Oggiano, G., 2010. A balanced foreland-hinterland deformation model for the southern Variscan belt of Sardinia, Italy. Geological Journal 45, 634–649.

Casini, L., Maino, M., Langone, A., Oggiano, G., Corvò, S., Reche-Estrada, J., Liesa, M., 2023. HT-LP metamorphism and fluid-fluxed melting during multi-stage anatexis of continental crust (N Sardinia, Italy). J. Metamorph. Geol. 41, 25–57.

Casini, L., Maino, M., Sanfilippo, A., Ildefonse, B., Dick, H.J.B., 2021. High-temperature strain localization and the nucleation of oceanic core complexes (16.5°N, mid-atlantic ridge). J. Geophys. Res. Solid Earth 126, e2021JB022215.

Chen, J., Jin, Z., Liu, W., Wang, Y., Zhang, J., 2021. Rheology of dry K-feldspar aggregates at high temperature and high pressure: an experimental study. Tectonophysics 817, 229072.

Cherniak, D.J., Dimanov, A., 2010. Diffusion in pyroxene, mica and amphibole. Rev. Mineral. Geochem. 72, 641–690.

Cocco, F., Funedda, A., 2019. The sardic phase: field evidence of ordovician tectonics in SE Sardinia, Italy. Geol. Mag. 156, 25–38. https://doi.org/10.1017/S0016756817000723.

Cocco, F., Loi, A., Funedda, A., Casini, L., Ghienne, J.-F., Pillola, G.L., Vidal, M., Meloni, M.A., Oggiano, G., 2023. Ordovician tectonics of the South European variscan realm: new insights from Sardinia. Int. J. Earth Sci. 112, 321–344. https://doi.org/10.1007/s00531-022-02250-w.

Cocco, F., Oggiano, G., Funedda, A., et al., 2018. Stratigraphic, magmatic and structural features of Ordovician tectonics in Sardinia (Italy): a review. J. Iber. Geol. 44 (4), 619–639. https://doi.org/10.1007/s41513-018-0075-1.

Conti, P., Carmignani, L., Funedda, A., 2001. Change of nappe transport direction during Variscan collisional evolution of central-southern Sardinia (Italy). Tectonophysics 332, 255–e273.

Conti, P., Carmignani, L., Oggiano, G., Funedda, A., Eltrudis, A., 1999. From thickening to extension in the Variscan belt e kinematic evidence from Sardinia (Italy). Terra. Nova 11, 93–99.

Conti, P., Funedda, A., Cerbai, N., 1998. Mylonite development in the hercynian basement of Sardinia (Italy). J. Struct. Geol. 20, 121e133.

Corvò, S., Maino, M., Langone, A., Schenker, F.L., Piazolo, S., Casini, L., Seno, S., 2021. Local variations of metamorphic record from compositionally heterogeneous rocks (Cima di Gagnone, Central Alps): inferences on exhumation processes of (U)HP-HT rocks. Lithos 390–391, 106126. https://doi.org/10.1016/j.lithos.2021.106126.

Cottle, J.M., Jessup, M.J., Newell, D.L., Searle, M.P., Law, R.D., Horstwood, M.S.A., 2007. Structural insights into the early stages of exhumation along an orogen-scale detachment: the South Tibetan detachment system, Dzakaa Chu section, eastern Himalaya. J. Struct. Geol. 29, 1781–1797.

Cross, A.J., Skemer, P., 2017. Ultramylonite generation via phase mixing in high-strain experiments. J. Geophys. Res. 122, 1744–1759.

De Bresser, J.H.P., Peach, C.J., Reijs, J.P.J., Spiers, C.J., 1998. On dynamic recrystallization during solid state flow: effects of stress and temperature. Geophys. Res. Lett. 25, 3457–3460.

Dell'Angelo, L.N., Tullis, J.A.N., 1988. Experimental deformation of partially melted granite aggregates. J. Metamorph. Geol. 6, 495–515.

Den Brok, B., 1996. The effect of crystallographic orientation on pressure solution in quartzite. J. Struct. Geol. 18, 859–860.

Dijkstra, A.H., Drury, M.R., Frijhoff, R.M., 2002. Microstructures and lattice fabrics in the Hilti mantle section (Oman Ophiolite): Evidence for shear localization and melt weakening in the crust–mantle transition zone? J. Geophys. Res. 107 (B11), 2270. https://doi.org/10.1029/2001JB000458.

Dimanov, A., Dresen, G., 2005. Rheology of synthetic anorthite-diopside aggregates: implications for ductile shear zones. J. Geophys. Res. 110, B07203 https://doi.org/10.1029/2004JB003431.

Dimanov, A., Ribacky, E., Hirth, G., Dresen, G., 2007. Creep and strain-dependent microstructures of synthetic Anorthite-diopside aggregates. J. Struct. Geol. 29, 1049–1069.

Dimanov, A., Lavie, M.P., Dresen, G., Ingrin, J., Jaoul, O., 2003. Creep of polycrystalline anorthite and diopside. J. Geophys. Res. 108 (B1), 2061. https://doi.org/10.1029/2002JB001815.

Dimanov, A., Xiao, X., Dresen, G., Wirth, R., 1999. Grain boundary diffusion creep of synthetic anorthite aggregates: the effect of water. J. Geophys. Res. 104, e10497, 10483.

Dong, H.W., Larson, K.P., Kellett, D.A., Xu, Z.Q., Li, G.W., Cao, H., Yi, Z.Y., Zeng, L.S., 2020. Timing of slip across the south Tibetan detachment system and yadong–gulu graben, eastern Himalaya. J. Geol. Soc. (Lond.) 178, jgs2019. –j2197.

Dumond, G., Mahan, K.H., Goncalves, P., Williams, M.L., Jercinovic, M.J., 2022. Monazite as a monitor of shear strain in orogenic crust. J. Struct. Geol. 161, 104672.

Fliervoet, T.F., White, S.H., Drury, M.R., 1997. Evidence for dominant grain-boundary sliding deformation in greenschist- and amphibolite-grade polymineralic ultramylonites from the Redbank Deformed Zone, Central Australia. J. Struct. Geol. 19, 1495e1520.

Fowler, R.H., Guggenheim, E.A., 1949. Statistical Thermodynamics. Cambridge University Press.

Fukunari, T., Wallis, S.R., 2007. Structural evidence for large-scale top-to-the-north normal displacement along the Median Tectonic Line in southwest Japan. Isl. Arc 16, 243–261.

Fusseis, F., Regenauer-Lieb, K., Liu, J., Hough, R.M., De Carlo, F., 2009. Creep cavitation can establish a dynamic granular fluid pump in ductile shear zones. Nature 459, 974–977. https://doi.org/10.1038/nature08051.

Gleason, G.C., Tullis, J., 1995. A flow law for dislocation creep of quartz aggregates determined with the molten salt cell. Tectonophysics 247, 1–23.

Gong, J.F., Ji, J.Q., Han, B.F., Chen, J.J., Sun, D.X., Li, B.L., Zhou, J., Tu, J.Y., Zhong, D. L., 2012. Early subduction-exhumation and late channel flow of the Greater Himalayan Sequence: implications from the Yadong section in the eastern Himalaya. Int. Geol. Rev. 54, 1184–1202.

Gomez Barreiro, J., Lonardelli, I., Wenk, H.R., Dresen, G., Rybacki, E., Ren, Y., Tomé, C. N., 2007. Preferred orientation of anorthite deformed experimentally in Newtonian creep. Earth Planet Sci. Lett. 264, 188–207.

Gratier, J.P., Guiguet, R., Renard, F., Jenatton, L., Bernard, D., 2009. A pressure solution creep law for quartz from indentation Experiments. J. Geophys. Res. B114, 03403.

Hacker, B.R., Yin, A., Christie, J.M., Davis, G.A., 1992. Stress magnitude, strain rate, and rheology of extended middle continental crust inferred from quartz grain sizes in the Whipple Mountains, California. Tectonics 11, 36–46. https://doi.org/10.1029/91TC01291.

Greenough, A.P., 1958. The deformation of metals by self-diffusion. Philos. Magazine 3, 1032–1041.

Hacker, B.M., Christie, J.M., 1990. Brittle/ductile and plastic/cataclastic transitions in experimentally deformed and metamorphosed amphibolite. In: Geophysical Monograph Series, vol. 56. American Geophysical Union, pp. 127–147.

Handy, M.R., 1994. Flow laws for rocks containing two non-linear viscous phases: a phenomenological approach. J. Struct. Geol. 16, 287–301.

Handy, M.R., Wissing, S.B., Streit, L.E., 1999. Frictional-viscous flow in mylonite with varied bimineralic composition and its effect on lithospheric strength. Tectonophysics 303, 175–191.

Hirth, G., Kohlstedt, D., 2003. Rheology of the upper mantle and the mantle wedge – a view from the experimentalists. In: Geophysical Monograph Series, vol. 138. American Geophysical Union, pp. 83–105.

Hirth, G., Tullis, J., 1992. Dislocation creep regimes in quartz aggregates. J. Struct. Geol. 14, 145–159.

Hofmeister, A.M., Mao, H.K., 2003. Pressure derivatives of shear and bulk moduli from the thermal Grüneisen parameter and volume-pressure data. Geochem. Cosmochim. Acta 67, 1207–1227.

Holyoke, C.W., Kronenberg, A.K., 2010. Accurate differential stress measurement using the molten salt cell and solid salt assemblies in the Griggs apparatus with applications to strength, piezometers and rheology. Tectonophysics 494, 17–31.

Hobbs, B.E., Ord, A., Ulrich, S., Schulmann, K., 2019. Rheology of mixed deformation mechanisms and mineral phase assemblages. J. Struct. Geol. 129, 103891.

Huet, B., Yamato, P., Grasemann, B., 2014. The Minimized Power Geometric model: An analytical mixing model for calculating polyphase rock viscosities consistent with experimental data. Journal of Geophysical Research, American Geophysical Union 119 (4), 3897–3924. https://doi.org/10.1002/2013JB010453.

Humphreys, F.J., Hatherly, M., 1995. Recrystallization and Related Annealing Phenomena. Pergamon, Oxford, p. 497.

Ichikawa, K., 1980. Geohistory of the median tectonic line of southwest Japan. Mem. Geol. Soc. Jpn. 18, 187–212.

Jamtveit, B., Petley-Ragan, A., Incel, S., Dunkel, K.G., Aupart, C., Austrheim, H., et al., 2019. The effects of earthquakes and fluids on the metamorphism of the lower continental crust. J. Geophys. Res. Solid Earth 0 (0). https://doi.org/10.1029/2018JB016461.

Ji, s., Martignole, J., 1994. Ductility of garnet as an indicator of extremely high temperature deformation. J. Struct. Geol. 16, 985–996.

Ji, S., Zhao, P., Xia, B., 2003. Flow laws of multiphase materials and rocks from end-members flow laws. Tectonophysics 370, 129–145. https://doi.org/10.1016/S0040-1951(03)00182-3.

Ji, S., 2004. A generalized mixture rule for estimating the viscosity of solid-liquid supensions and mechanical properties of polyphase rocks and composite materials. J. Geophys. Res. 109, B10207 https://doi.org/10.1029/2004JB003124.

Karato, S., Toriumi, M., Fujii, T., 1980. Dynamic recrystallization of olivine single crystals during high-temperature creep. Geophys. Res. Lett. 7, 649–652.

Jiang, Y., Zang, S., Wei, R., 2005. Decibel error test and flow law of multiphase rocks based on energy dissipation theory. Earth Planet. Sci. Lett. 235, 200–210.

Karato, S., Paterson, M.S., Fitz Gerald, J.D., 1986. Rheology of synthetic olivine aggregates: influence of grain-size and water. J. Geophys. Res. 91, 8151–8176.

Karato, S., Wang, Z., Liu, B., Fujino, K., 1995. Plastic deformation of garnets: systematics and implications for the rheology of the mantle transition zone. Earth Planet Sci. Lett. 130, 13–30.

Katori, T., Shigematsu, N., Kameda, J., Miyakawa, A., Matsumura, R., 2021. 3D fault-zone architecture across the brittle–plastic transition along the Median Tectonic Line, SW Japan: fault-rock characterization. J. Struct. Geol. 153, 104446.

Kilian, R., Heilbronner, R., Stüniz, H., 2011. Quartz grain size reduction in granitoid rocks and the transition from dislocation to diffusion creep. J. Struct. Geol. 33, 1265–1284. https://doi.org/10.1016/j.jsg.2011.05.004.

Kubota, Y., Takeshita, T., Yagi, K., Itaya, T., 2020. Kinematic analyses and radiometric dating of the large–scale Paleogene two–phase faulting along the Median Tectonic Line, southwest Japan. Tectonics 39, 1–29.

Langdon, T.G., Mohamed, F.A., 1976. Deformation mechanism maps for ceramics. J. Mater. Sci. 11, 317–327.

Langdon, T.G., 2006. Grain boundary sliding revisited: developments in sliding over four decades. J. Mater. Sci. 41, 597–609. https://doi.org/10.1007/s10853-006-6476-0.

Langone, A., Gueguen, E., Prosser, G., Caggianelli, A., Rottura, A., 2006. The Curinga-Girifalco fault zone (northern Serre, Calabria) and its significance within the Alpine tectonic evolution of the western Mediterranean. J. Geodyn. 42, 140–158.

Lifshitz, I.M., 1963. On the theory of diffusion-viscous flow of polycrystalline bodies. Sov. Phys. - JETP 17 (4), 909.

Lister, G.S., Price, G.P., 1978. Fabric development in a quartz-feldspar mylonite. Tectonophysics 49, 37–78.

Loi, A., Cocco, F., Oggiano, G., Funedda, A., Vidal, M., Ferretti, A., Leone, F., Barca, S., Naitza, S., Ghienne, J.-F., Pillola, G.L., 2023. The Ordovician of Sardinia (Italy): from the 'Sardic Phase' to the End-Ordovician Glaciation, Palaeogeography and Geodynamic Context, vol. 523. Geological Society of London. https://doi.org/10.1144/sp532-2022-121. S. P.

Lopez-Sanchez, M.A., Llana-Fúnez, S., 2015. An evaluation of different measures of dynamically recrystallized grain size for paleopiezometry or paleowattometry studies. Solid Earth 6, 475–495. https://doi.org/10.5194/se-6-475-2015.

Mares, V.M., Kronenberg, A.K., 1993. Experimental deformation of muscovite. J. Struct. Geol. 9/10, 1061–1075.

Matthies, S., Humbert, M., 1993. The realization of the concept of a geometric mean for calculating physical constants of polycrystalline materials. Phys. Status Solidi B 177, K47–K50.

McGarr, A., 1980. Some constraints on levels of shear stress in the crust from observations and theory. J. Geophys. Res. 85 (B11), 6231–6238.

Mehl, L., Hirth, G., 2008. Plagioclase preferred orientation in layered mylonites: evaluation of flow laws for the lower crust. J. Geophys. Res. Solid Earth 113, B05202. https://doi.org/10.1029/2007JB005075.

Melosh, B.L., Rowe, C.D., Gerbi, C., Smit, L., Macey, P., 2018. Seismic cycle feedbacks in a mid-crustal shear zone. J. Struct. Geol. 112, 95–111.

Miranda, E.A., Hirth, G., John, B.E., 2016. Microstructural evidence for the transition from dislocation creep to dislocation-accommodated grain boundary sliding in naturally deformed plagioclase. J. Struct. Geol. 92, 30–45. https://doi.org/10.1016/j.jsg.2016.09.002.

Moghadam, R.H., Trepmann, C.A., Stöckhert, B., Renner, J., 2010. Rheology of synthetic omphacite aggregates at high pressure and high temperature. J. Petrol. 51, 921–945.

Mohamed, F.A., Langdon, T.G., 1975. Deformation mechanism maps for solid solution alloys. Scr. Metall. 9, 137–140.

Montesi, L.G.J., 2007. A constitutive model for layer development in shear zones near the brittle-ductile transition. Geophys. Res. Lett. 34, L08307.

Montesi, L.G.J., Hirth, G., 2003. Grain size evolution and the rheology of ductile shear zones: from laboratory experiments to post-seismic creep. Earth Planet Sci. Lett. 211, 97–110. https://doi.org/10.1016/S0012-821X(03)00196-1.

Mukherjee, S., 2012. Simple shear is not so simple! Kinematics and shear senses in Newtonian viscous simple shear zones. Geol. Mag. 149, 819–826.

Newman, J., Lamb, V.M., Drury, M.R., Vissers, R.L.M., 1999. Deformation processes in a peridotite shear zone: Reaction-softening by an H2O-deficient, continuous net transfer reaction. Tectonophysics 303 (1), 193–222.

Okudaira, T., Shigematsu, N., 2012. Estimates of stress and strain rate in mylonites based on the boundary between the fields of grain-size sensitive and insensitive creep. J. Geophys. Res. 117, 1–15.

Ortolano, G., Fazio, E., Visalli, R., Alsop, I.G., Pagano, M., Cirrincione, R., 2020. Quantitative microstructural analysis of mylonites formed during Alpine tectonics in the western Mediterranean realm. J. Struct. Geol. 131, 103956.

Orzol, J., Stöckhert, B., Trepmanmn, C.A., Rummel, F., 2006. Experimental deformation of synthetic wet jadeite Aggregates. J. Geophys. Res. 111, B06205.

Paul, B., 1959. Prediction of Elastic Constants of Multi-phase Materials. Division of Engineering, Brown University.

Platt, J.P., Behr, W.M., 2011a. Grain size evolution in ductile shear zones: implications for strain localization and the strength of the lithosphere. J. Struct. Geol. 39, 127–130. https://doi.org/10.1016/j.jsg.2011.01.018.

Platt, J.P., Behr, W.M., 2011b. Lithospheric shear zones as constant stress experiments. Geology 33, 537–550. https://doi.org/10.1130/G31561.1.

Platt, J.P., Behrmann, J.H., 1986. Structures and fabrics in a crustal-scale shear zone, Betic Cordillera, SE Spain. J. Struct. Geol. 8, 15–33.

Poirier, J.-P., 1985. Creep of Crystals. Cambridge University Press, Cambridge, p. 260.

Post, A., Tullis, J., 1999. A recrystallized grain size piezometer for experimentally deformed feldspar aggregates. Tectonophysics 303, 159–173.

Précigout, J., Gueydan, F., Gapais, D., Garrido, C.J., Essaifi, A., 2007. Strain localization in the subcontinental mantle – a ductile alternative to the brittle mantle. Tectonophysics 445, 318–336. https://doi.org/10.1016/j.tecto.2007.09.002.

Précigout, J., Prigent, C., Palasse, L., Pochon, A., 2017. Water pumping in mantle shear zones. Nat. Commun. 8, 15736.

Ranalli, G., 1995. *Rheology of the Earth*. Chapman and Hall, London, p. 413.

Rast, M., Ruh, J.B., 2021. Numerical shear experiments of quartz-biotite aggregates: insights on strain weakening and two-phase flow laws. J. Struct. Geol. 149, 104375.

Reuss, A., 1929. Berechnung der Fliessgrenze von Mischkristallen auf Grund der Plastizitäts bedingung für Einkristalle. Z. Angew. Math. Mech. 9, 49–58.

Robie, R.A., Bethke, P.M., 1962. Molar volumes and densities of minerals. In: Trace Elements Investigations, vol. 822. US Geological Survey. https://doi.org/10.3133/70159012.

Rosenberg, C.L., Handy, M.R., 2005. Experimental deformation of partially melted granite revisited: implications for the continental crust. J. Metamorph. Geol. 23, 19–28.

Rutter, E.H., 1995. Experimental study of the influence of stress, temperature, and strain on the dynamic recrystallization of Carrara marble. J. Geophys. Res. 100, 24651–24663.

Rutter, E.H., Brodie, K.H., 2004. Experimental grain size-sensitive flow of hot-pressed Brazilian quartz aggregates. J. Struct. Geol. 26, 2011–2023.

Rybacki, E., Paterson, M., Wirth, R., Dresen, G., 2003. Rheology of calcite-quartz aggregates deformed to large strain in torsion. J. Geophys. Res. 108, 2089. https://doi.org/10.1029/2002JB001833.

Rybacki, E., Wirth, R., Dresen, G., 2010. Superplasticity and ductile fracture of synthetic feldspar deformed to large strain. J. Geophys. Res. 115, B08209 https://doi.org/10.1029/2009JB007203.

Schmid, S.M., Paterson, M.S., Boland, J.N., 1980. High temperature flow and dynamic recrystallization in Carrara marble. Tectonophysics 65, 245–280.

Searle, M.P., Parrish, R.R., Hodges, K.V., Hurford, A., Ayres, M.W., Whitehouse, M.J., 1997. Shisha Pangma leucogranite, south Tibetan Himalaya: field relations, geochemistry, age, origin, and emplacement. J. Geol. 105, 295–317.

Shigematsu, N., Kametaka, M., Inada, N., Miyawaki, M., Miyakawa, A., Kameda, J., Togo, T., Fujimoto, K., 2017. Evolution of the median tectonic line fault zone, SW Japan, during exhumation. Tectonophysics 696, 52–69.

Shimizu, I., 2008. Theories and applicability of recrystallized grain-size piezometers: the role of dynamic deformation mechanisms. J. Struct. Geol. 30, 899–917.

Sibson, R.H., 1982. Fault zone models, heat flow, and depth distribution of earthquakes in the continental crust of the United States. Bull. Seismol. Soc. Am. 72, 151–161.

Sibson, R.H., 1980. Transient discontinuities in ductile shear zones. J. Struct. Geol. 2, 165–171.

Simpson, C., 1985. Deformation of granitic rocks across the brittle-ductile transition. J. Struct. Geol. 7, 503–511.

Stipp, M., Tullis, J., 2003. The recrystallized grain size piezometer for quartz. Geophys. Res. Lett. 30, 2088. https://doi.org/10.1029/2003GL018444.

Stipp, M., Tullis, J., Behrens, H., 2006. Effect of water on the dislocation creep microstructure and flow stress of quartz and implications for the recrystallized grain size piezometer. J. Geophys. Res. 111, B04201 https://doi.org/10.1029/2005JB003852.

Stipp, M., Tullis, J., Scherwath, M., Behrmann, J.H., 2010. A new perspective on paleopiezometry: dynamically recrystallized grain size distributions indicate mechanism changes. Geology 38, 759–762.

Spann, H., Brudy, M, Fuchs, K, 1991. Stress evaluation in offshore regions of Norway. Terra Nova 3, 148–152.

Speciale, P.A., Tokle, L., Behr, W.M., 2022. Feldspar and orthopyroxene piezometers constrained using quartz-feldspar and olivine-orthopyroxene mineral pairs from natural mylonites. J. Struct. Geol. 154, 104495.

Stünitz, H, Tullis, J, 2001. Weakening and strain localization produced by syn-deformational reaction of plagioclase. International Journal of Earth Sciences 90, 136–148.

Ter Heege, J.H., De Bresser, J.H.P., Spiers, C.J., 2004a. Composite flow laws for crystalline materials with log-normally distributed grain size: theory and application to olivine. J. Struct. Geol. 26, 1693–1705.

Ter Heege, J.H., De Bresser, J.H.P., Spiers, C.J., 2004b. Dynamic recrystallization of wet synthetic polycrystalline halite: dependence of grain size distribution on flow stress, temperature and strain. Tectonophysics 396, 35–57.

Till, J.L., Moskowitz, B., 2013. Magnetite deformation mechanism maps for better prediction of strain partitioning. Geophys. Res. Lett. 40, 697–702.

Till, J.L., Rybacki, E., 2020. High-temperature creep of magnetite and ilmenite single crystals High-temperature creep of magnetite and ilmenite single crystals. Phys. Chem. Miner. 47 (2020), 52.

Tokle, L., Hirth, G., Behr, W.M., 2019. Flow laws and fabric transitions in wet quartzite. Earth Planet Sci. Lett. 505, 152–161.

Tullis, T.E., Horowitz, F.G., Tullis, J., 1991. Flow laws of polyphase aggregates from end-member flow laws. J. Geophys. Res. 96, 8081–8096.

Twiss, R.J., 1977. Theory and applicability of a recrystallized grain size paleopiezometer. Pure Appl. Geophys. 115, 227–244.

van der Wal, D., Chopra, P., Drury, M., Fitz Gerald, J., 1993. Relationships between dynamically recrystallized grain size and deformation conditions in experimentally deformed olivine rocks. Geophys. Res. Lett. 20, 1479–1482.

Van der Werf, T., Chatzaras, V., Kriegsman, L.M., Kronenberg, A., Tikoff, B., Drury, M.R., 2017. Constraints on the rheology of the lower crust in a strike-slip plate boundary: evidence from the San Quintín xenoliths, Baja California, Mexico. Solid Earth 8, 1211–1239.

Vissers, R.L.M., Drury, M.R., Hoogerduijn Starting, E.H., Spiers, C.J., van der Wal, D., 1995. Mantle shear zones and their effect on lithosphere strength during continental breakup. Tectonophysics 249, 155–171.

Voigt, W., 1928. Lehrbuch der Kristallphysik. Teubner, Leipzig.

Zener, C., 1951. Theory of D0 for atomic diffusion in metals. J. Appl. Phys. 22, 372–375.

Zhang, L., Zhang, B., Zhang, J., Wang, J., Cai, F., Zhao, Z., Chen, S., Li, X., 2022. The rheology and deformation of the South Tibetan Detachment System as exposed at Zherger La, east-central Himalaya: implications for exhumation of the Himalayan metamorphic core. J. Struct. Geol. 157, 104559.

Zhou, B., Liu, J., Chen, X., Hou, C., 2022. Fluid-enhanced grain-size reduction of K-feldspar from a natural middle crustal shear zone in northern Beijing, China. Tectonophysics 838. https://doi.org/10.1016/j.tecto.2022.229478.

Zoback, M.D., Harjes, H.P., 1997. Injection-induced earthquakes and crustal stress at 9 km depth at the KTB deep drilling site, Germany. J. Geophys. Res. 102 (B8), 18477–18491.